Three-dimensional transient rip currents: Bathymetric excitation of low-frequency intrinsic variability

Uchiyama, Yusuke
McWilliams, James C.
Akan, Cigdem

(Citation)
Journal of Geophysical Research: Oceans,122(7):5826-5849

(Issue Date)
2017-07

(Resource Type)
journal article

(Version)
Version of Record

(URL)
https://hdl.handle.net/20.500.14094/90004437

AGU PUBLICATIONS

JGR

Journal of Geophysical Research: Oceans

RESEARCH ARTICLE

10.1002/2017JC013005

Three-dimensional transient rip currents: Bathymetric excitation of low-frequency intrinsic variability

Yusuke Uchiyama[1,2,3], James C. McWilliams[2], and Cigdem Akan[2]

[1]Department of Civil Engineering, Kobe University, Kobe, Japan, [2]Department of Atmospheric and Oceanic Sciences, University of California, Los Angeles, California, USA, [3]Coastal and Estuarine Environmental Department, Port and Airport Research Institute, Yokosuka, Japan

Key Points:
- The ROMS-WEC model is applied to analyze 3-D turbulent rip currents containing significant very low frequency motions (VLFs)
- The intrinsic VLFs are excited on realistic bathymetries under steady, uniform incident offshore wave conditions
- Three-dimensionality, the current effects on waves (CEW), and bathymetric and forcing conditions on the intrinsic VLFs are investigated

Correspondence to:
Y. Uchiyama,
uchiyama@harbor.kobe-u.ac.jp

Citation:
Uchiyama, Y., J. C. McWilliams, and C. Akan (2017), Three-dimensional transient rip currents: Bathymetric excitation of low-frequency intrinsic variability, *J. Geophys. Res. Oceans*, *122*, 5826–5849, doi:10.1002/2017JC013005.

Received 24 APR 2017
Accepted 19 JUN 2017
Accepted article online 5 JUL 2017
Published online 25 JUL 2017

Abstract The ROMS-WEC model [*Uchiyama et al.*, 2010] based on an Eulerian wave-averaged vortex-force asymptotic theory of McWilliams et al. (2004) is applied to analyze 3-D transient wave-driven rip currents and associated intrinsic very low-frequency (VLF) variability in the surf zone on a surveyed bathymetry under spatiotemporally uniform offshore incident waves. The 3-D rip currents are substantially depth-dependent due to the vertical recirculation, composed of pairs of counter-rotating longitudinal overturning roll cells that promote surface convergence. The vortex force plays an important role in vorticity budget, preconditioning overall vorticity reduction. These rip currents are intrinsically unstable and contribute about 70% to kinetic energy (KE) as eddy kinetic energy (EKE), consistent with observations. The dominant fluctuation period fits the VLF band, at about 18 min. The current effect on waves (CEW) alters not only the mean rip structure, but also the associated turbulence as the modified cross-shore EKE profile with considerable accentuation in the inner surf zone. Increased alongshore bathymetric variability proportionally intensifies KE and intrinsic EKE, whereas it reduces the VLF period. With a guide of a pseudo 2D model, we reveal that vortex tilting effect due to the horizontal vorticity inherent in the 3-D rip currents promotes collapse of the 3-D eddies through an enhanced forward kinetic energy cascade, leading to short-lived, laterally-stretched 3-D eddies resulting in elongated filaments that decay more quickly than coherent, long-lived, circular 2-D eddies.

1. Introduction

Surf zones act as a barrier between inner-shelf and shoreline by wave-driven littoral currents. However, the surf zone retention is occasionally collapsed by offshore-headed rip currents [*Reniers et al.*, 2009], resulting in horizontal circulation referred to as rip cells [e.g., *Bowen*, 1969]. Rip currents are associated with vortex shedding due to lateral shear and thus are readily unstable [*Kennedy*, 2003; *Haller and Dalrymple*, 2001] as have been observed in numerical models, laboratories and field experiments [e.g., *Sonu*, 1972; *Aagaard et al.*, 1997; *Brander and Short*, 2001; *Haas and Svendsen*, 2002; *Yu and Slinn*, 2003; *MacMahan et al.*, 2005; *Reniers et al.*, 2009]. Rip current pulsations under near-normal wave incidence and alongshore-propagating shear waves [e.g., *Oltman-Shay et al.*, 1989] under oblique wave incidence occur intermittently or quasi-periodically based on both observations [*MacMahan et al.*, 2004a,2004b] and theoretical works [*Haller and Dalrymple*, 2001; *Yu*, 2006]. The vortical motions in the littoral currents are expected to occur at significantly lower frequencies ($f < 0.004$ Hz) than infragravity waves ($0.004\ \text{Hz} < f < 0.04$ Hz). They are often referred to as very low frequency motions (VLFs), because of the vortical motions at time scales of O (1–10) minutes induced by (1) shear instabilities [e.g., *Özkan-Haller and Kirby*, 1999; *Haller and Dalrymple*, 2001; *Noyes et al.*, 2004], (2) wave groups [*Sonu*, 1972; *MacMahan et al.*, 2004a; *Long and Özkan-Haller*, 2009], and (3) vortical forcing due to individual breaking waves [e.g., *Spydell and Feddersen*, 2009; *Feddersen*, 2014]. The shear instability is well explained and represented as an inflection point, normal mode instability of a specified current profile [cf. *Bowen and Holman*, 1989; *Dodd et al.*, 1992, 1994, 2000; *Allen et al.*, 1996; *Reniers et al.*, 1997]. In turn, the influences of wave groups have typically been interpreted in relation to changes in mass flux associated with the incident groups themselves [*Munk*, 1949] or infragravity waves generated by the wave groups [*Sonu*, 1972; *MacMahan et al.*, 2004a]. *Reniers et al.* [2007] suggested from a two-way coupled, time-dependent phase-averaged wave and barotropic circulation model on a rip-channeled beach that the group scale forcing is substantial to excitation of VLFs. These VLFs are most energized by directionally broad random waves in the surf zone, and they rapidly decay in the offshore direction just outside the surf zone.

Long and Özkan-Haller [2009] reported with a similar model that random wave group forcing significantly broadens frequency-wavenumber velocity spectra of shear wave for alongshore-uniform bathymetry. The consequent wave-forcing field appears as patches with alongshore length scales of *O* (100) m, leading to transient vortical lateral torque on the scale of the rip-channel spacing. The similar conclusion has been drawn from *Spydell and Feddersen* [2009], *Feddersen et al*. [2011], and *Feddersen* [2014], who demonstrated that VLFs are excited as intensely as observations, as a consequence of wave-breaking eddy generation in a phase-resolving, barotropic Boussinesq model with directionally spread, random incident waves on an alongshore-uniform beach. Such a stochastic wave forcing also stimulates transient rip currents in a phase-averaged 3-D model [*Kumar and Feddersen*, 2017a]. A consensus is being achieved such that the transient irrotational forcing due to group waves and/or randomness of finite-crest length wave breaking is responsible for a part of VLFs (hereinafter, "forced" VLFs). Nevertheless, alongshore-uniform bathymetry is not the optimal test bed to measure spontaneous VLFs ("intrinsic" VLF) because it does not provoke alongshore-variable vortical torque due to wave breaking, which is a main source of the intrinsic VLFs [*Geiman and Kirby*, 2013].

The feedback mechanisms of the current effect on waves (CEW) [cf. *Uchiyama et al*., 2009, hereinafter UMR09], consisting of the frequency Doppler shifting and refraction of primary wave on ambient phase-averaged currents and surface elevation (*viz*., wave set-up/down), is anticipated to alter VLFs because it is known to attenuate instabilities of shear waves [*Özkan-Haller and Li*, 2003; UMR09] and rip currents [*Yu and Slinn*, 2003; *Haas et al*., 2003; *Weir et al*., 2011]. Bottom drag is another important factor determining the stability limits [e.g., *Bowen and Holman*, 1989; *Haas et al*., 2003]. Wave-driven currents are generally accompanied by strong vertical shear due to vertically recirculating flows caused by surface-intensified, shoreward breaker acceleration that primarily balances with cross-shore pressure gradient to promote seaward undertow currents confined near the bed [cf. *Uchiyama et al*., 2010, hereinafter UMS10]. While bottom boundary layer streaming acceleration is of second importance to surf-zone dynamics, it is essential to near-bed offshore transport of negatively buoyant larvae [*Fujimura et al*., 2014]. Rip currents are also observed to have significant vertical structure [*Haas and Svendsen*, 2002; *MacMahan et al*., 2005]. The vorticity around the surf zone promotes a nontrivial vortex force particularly in the alongshore direction interplayed with Stokes drift [*Kumar et al*., 2012; *Kumar and Feddersen*, 2017a]. Therefore, 3-D wave-averaged circulation models based on a vortex force formalism [*McWilliams et al*., 2004, hereinafter MRL04] with CEW are inevitable for conducting this type of study, whereas most of the numerical studies have been conducted with a depth-averaged (i.e., barotropic), 2-D wave-averaged model, based on the classical radiation stress formalism [e.g., *Longuet-Higgins and Stewart*, 1962; *Hasselmann*, 1971; *Phillips*, 1977].

Among a limited number of the numerical studies on the 3-D transient littoral currents, *Reniers et al*. [2009] extended their earlier work based on a barotropic framework [*Reniers et al*., 2007] by exploiting the Delft3D model [*Walstra et al*., 2000; *Lesser et al*., 2004], forced by a spectral peak WKB wave model operated on the wave group timescale. They successfully reproduced the combined forced and intrinsic VLFs for the periods of 4–60 min in the rip current during the *RCEX* field experiment on the surveyed variable bathymetry [*MacMahan et al*., 2010a] and further described lateral mixing efficiency as a Lagrangian coherent structure depicted by the finite-time Lyapunov exponent [*Reniers et al*., 2010]. *Geiman et al*. [2011] compared the result of *Reniers et al*. [2009] with that from the phase-resolving 2-D Boussinesq model for the *RCEX* data and reported that both the models yielded comparable Lagrangian mixing efficiency such as absolute and pair separations, consistent with the observations. *Marchesiello et al*. [2015] applied the two-way coupled WKB spectral peak wave model with the 3-D circulation model developed in UMS10 to transient rip currents on Biscarrosse Beach, France. They successfully reproduced energetic intrinsic VLFs at *O* (10) minutes, mainly driven by slowly modulating waves on timescales of *O* (1–2) hours due to tides and wind. The aforementioned study of *Kumar and Feddersen* [2017a] utilized a wave-averaged 3-D circulation model forced by stochastically breaking directional waves on an alongshore-uniform planar beach to evaluate cross-shelf transition of the mixing efficiency due to the forced VLFs in transient rip currents. *Newberger and Allen* [2007] examined the intrinsic VLFs in 3-D shear waves during the *DUCK94* field experiment. They pointed out that 3-D shear waves are more stable than 2-D, consistent with the result from a quasi-3-D model [*Zhao et al*., 2003], and that omission of the vortex force term and CEW increase the errors in the alongshore velocity.

However, 3-D numerical studies on the transient rip currents in the surf zone have not been extensively conducted yet to fully answer questions such as: What is the 3-D nature of the transient rip currents? Is

bathymetric variability essential in promoting the 3-D intrinsic VLFs? What controls the excitation of the intrinsic VLFs? How and why are the 3-D intrinsic VLFs different from the 2-D ones? In the present study we aim to answer those questions by using a 3-D numerical framework, ROMS-WEC (UMS10), which is a wave-averaged version of ROMS (Regional Oceanic Modeling System) [*Shchepetkin and McWilliams*, 2005, 2008] based on a vortex force formalism of MRL04, tightly coupled with a spectral peak WKB wave refraction model. Three-dimensional numerical experiments are conducted for turbulent rip currents driven by normal incident waves. The ROMS-WEC model has been adapted to 3-D coastal applications with prevailing wave-driven currents, showing quite good agreements with measurements [cf. *Marchesiello et al*., 2015; *Kumar et al*., 2015]. We show here that time-invariant and spatially homogeneous offshore incident waves, which are not expected to induce the forced VLFs, excite 3-D turbulent rip currents on timescales of O (1–10) minutes on an immobile beach with realistic spatial bathymetric variability ubiquitous in nature. Our focus is on the intrinsic part of the VLFs, yet the forced VLFs usually contain equivalent turbulence intensity [e.g., *Reniers et al*., 2007] or enstrophy [e.g., *Long and Özkan-Haller*, 2009] with that in the intrinsic VLFs. We further demonstrate rip currents are spontaneous for spatially variable bathymetry with alongshore undulations, resulting in unstable motions that contain significantly energetic intrinsic VLFs, comparable to those measured during the *SandyDuck* field campaign [*MacMahan et al*., 2010b; *de Schipper et al*., 2012] without wave groups and random wave breaking. Supplemental simulations are carried out to examine influences from three-dimensionality, alongshore variability in the bathymetry, wave-current interaction (i.e., CEW), and different forcing conditions on the intrinsic VLFs.

The remainder of the paper is organized as follows. The numerical model and experimental configuration are described in section 2, supplemented by Appendices. Section 3 demonstrates 3-D transient rip currents containing significant intrinsic VLFs are driven by steady, normal incident waves for the surveyed beach bathymetry. In section 4, the eddy generation mechanism is discussed through the eddy statistic analysis and the barotropic vorticity budget analysis, followed by a series of model experiments to demonstrate modification of the intrinsic VLFs in response to CEW, amplitudes of bathymetric variability, and forcing conditions. A comparative spin-down experiment for decaying processes of the initially forced eddies in rip currents is presented in section 5 to further examine 3-D effects on the fate of eddies. Section 6 gives conclusions.

2. Methods

2.1. The ROMS-WEC Model

The ROMS-WEC model [*Uchiyama et al*., 2010; UMS10] is a 3-D wave-averaged ocean circulation model based on a terrain-following, hydrostatic ocean model, ROMS [e.g., *Shchepetkin and McWilliams*, 2005, 2008], which accounts for the interaction of surface gravity waves and currents with a vortex force formalism. Eulerian wave-averaged conservation equations for mass, momentum, and tracers are included in the ROMS based on an asymptotic theory of MRL04, where conservative WEC (wave effects on currents) include the vortex force, the Stokes-Coriolis force, Bernoulli head, and quasi-static pressure and sea-level responses. The ROMS-WEC further considers nonconservative WEC due to wave breaking, associated surface roller waves, bottom streaming, wave-enhanced vertical mixing, and wave-enhanced bottom drag suitable to coastal and nearshore applications (Appendix A). The ROMS-WEC model was applied to 3-D transient rip currents, and validated against in situ wave field observed by a video imaging technique [*Holman and Haller*, 2013] and the ADCP data in *Marchesiello et al*. [2015].

The depth-averaged, barotropic 2-D model is configured and operated as the stand-alone model, based on the barotropic mode of the ROMS-WEC by omitting the barotropic-baroclinic coupling requisite for fully 3-D simulations (Appendix B). The boundary conditions and our choice of the submodels such as the bottom drag prescription are provided in Appendix C. Both of the 3-D and barotropic 2-D ROMS-WEC models are tightly coupled with the built-in spectrum-peak WKB wave-refraction model that takes into account the effect of currents on waves (CEW) as described in Appendix D.

2.2. The Experimental Setup

The ROMS-WEC model is applied to transient rip currents on a realistic beach bathymetry driven by steady, time-invariant, alongshore-uniform normal incident offshore waves. We choose a surveyed bathymetry near the Field Research Facility (FRF) in Duck, NC, on 22 February 2010, when a pronounced rip channel emerged

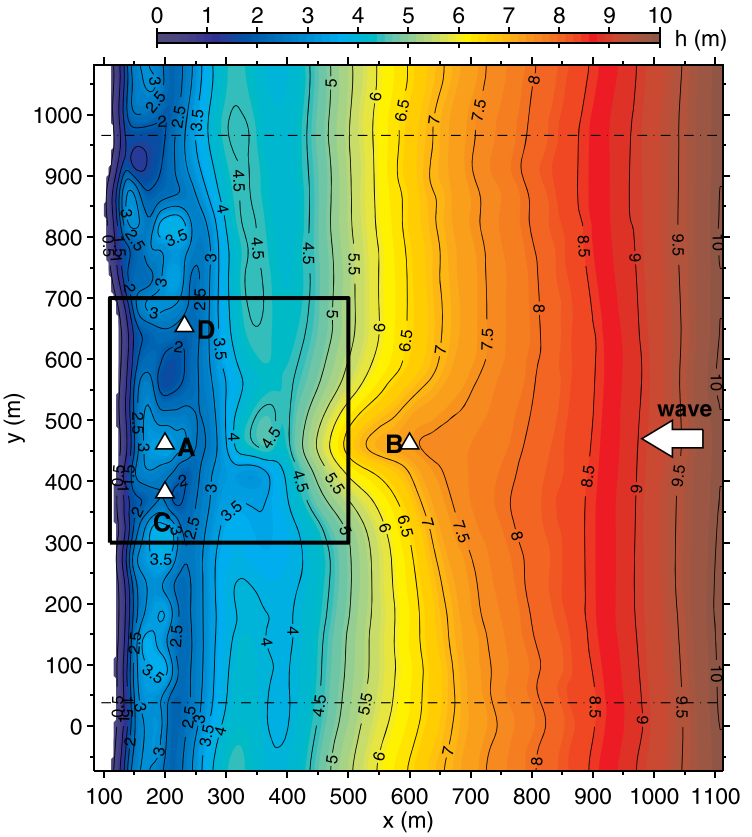

Figure 1. Model bathymetry showing the entire model domain used in the present study, representing a sandy beach at Duck, NC, based on the surveyed bathymetry on 22 February 2010. The horizontal coordinate follows the definition relative to Field Research Facility (FRF) of U.S. Army Corps of Engineers. Contours with colors show depth h (m). The black thick rectangle is the blow-up region used in Figure 3. Open triangles are four monitoring stations A–D in Figure 6. The dash-dot lines represent the boundaries outward from which bathymetries are blended for the alongshore periodicity.

near the 613 m-long FRF pier at around $y = 460$ m (Figure 1). The beach is double-barred with the bathymetric peaks approximately located for $220 \leq x \leq 280$ m (the inner bar) and $360 \leq x \leq 420$ (the outer bar). The model domain extends laterally to 1,024 m offshore × 1,152 m northward with uniform grid spacing and 20 stretched vertical s-layers (Table 1). We also carry out a supplemental barotropic 2-D simulation for the same bathymetric and forcing conditions. We show the results forced by the time-invariant offshore incident waves with the RMS wave height H_{rms} of 1.2 m, the peak wave period T_p of 10 s, and the peak wave direction θ_p of 0° as the offshore clamped boundary condition of the WKB wave model (Appendix D). The feedback mechanism of CEW is always taken into account unless otherwise stated. Although the ROMS-WEC accounts for buoyancy effects by solving the wave-averaged heat and salinity conservation equations and the equation of state, we assume constant density in the present study. The imposed external forcing only comes from steady and uniform incident waves. Other forcing such as surface wind stress, heat, and freshwater fluxes are all omitted. The Coriolis and Stokes-Coriolis terms are also neglected because of the small domains and the short time scales. The surface roller model (Appendix D) is not activated to avoid further complexity. We leave these terms and equations merely for the completeness. No additional lateral mixing is introduced except for small hyper diffusion inherent in the third order upstream-biased advection scheme of ROMS.

The resting ocean is assumed initially and offshore waves are imposed instantaneously at $t = 0$. Because instability intrinsically takes place immediately after the initialization from the resting state, neither random noise nor initial ramping of the wave forcing is imposed as was done in the shear wave experiment in UMR09. The baroclinic and barotropic time steps are typically 1 sec and 0.15 s. The model output occurs every minute until $t = 600$ min. The analyses are mostly performed for $100 \leq t \leq 600$ min to exclude the initial adjustment and spin-up effects. Note that the results shown below are quite robust qualitatively even with different incident wave and bathymetric conditions unless the incident angle $|\theta_p| > 3°$.

Table 1. Model Configuration

Grid cells	256 × 288 × vertical 20 layers
Grid spacing	$\Delta x = \Delta y = 4$ m
s-coordinate parameters	$\theta_s = \theta_b = 5$, h_c=2.0 m
Incident wave height, H_{rms}	1.2 m
Incident wave period, T_p	10.0 s
Incident wave angle, θ_p	0° (to W)
Non-wave surface elevation, ζ	0 m
CT breaking parameters	$B_b = 1.3$, $\gamma_b = 0.38$

3. Transient 3-D Rip Currents

3.1. Mean Cross-Shore Profiles

Figure 2 shows cross-shore profiles of the time- and alongshore-averaged (denoted by $\langle\cdot\rangle$) waves, barotropic current $\mathbf{u}_{bt}$, and barotropic Stokes drift $\mathbf{u}_{bt}^{St}$,

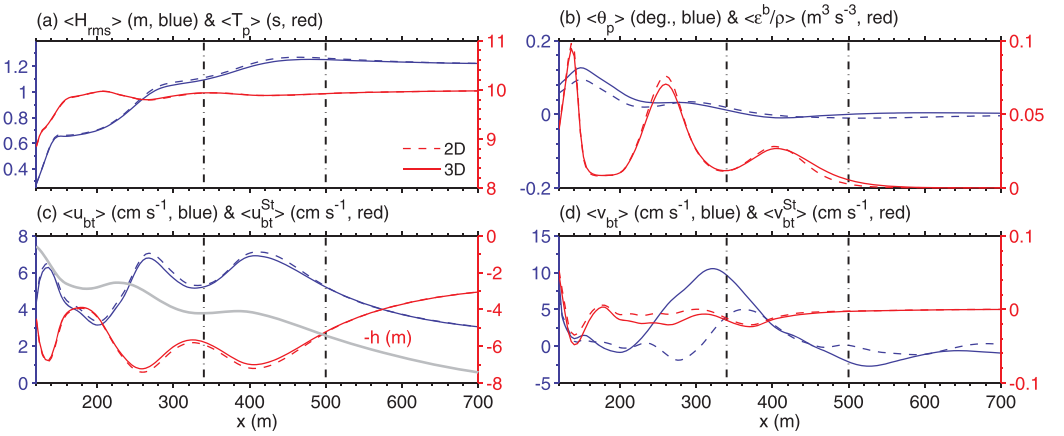

Figure 2. Cross-shore profiles of time- and alongshore-averaged (denoted by the $\langle\cdot\rangle$ operator) model results forced by steady offshore waves with the RMS wave height H_{rms} of 1.2 m, the peak wave period T_p of 10 s, and the peak wave direction θ_p of 0° (normal incidence) for the fully 3-D (solid lines) and the barotropic 2-D (dotted lines) cases: (a) H_{rms} (blue lines) and T_p (red lines), (b) θ_p (blue) relative to the shore-normal direction and the kinematic breaker dissipation rate ϵ^b/ρ (red), and (c) the cross-shore (offshore) and (d) the alongshore (northward) components of the barotropic velocity $\mathbf{u}_{bt}$ (blue) and barotropic Stokes drift $\mathbf{u}_{bt}^{St}$ (red). Notice the line color corresponds to that of the *y* axis and its labels. The thick gray line in Figure 2c represents the alongshore-averaged bathymetry, *-h* (m), which shares the labels on the right red axis. The two vertical dashed lines denote the approximate offshore extents of the inner ($x < 340$ m) and outer ($340 \le x < 500$ m) surf zones.

from the 3-D and 2-D models. The alongshore-averaged bathymetry is overlaid with the thick gray curve in (c). The mildly sloping beach with a mean slope of about 1/100 has two plateaus segmented by two long-shore bars peaked at around $x = 240$ (the inner bar) and 400 m (the outer bar). The wave fields are almost identical in the 2-D and 3-D models. Depth-induced breaking ϵ^b peaks at three locations with the maximum appearing in the vicinity of the shoreline and the others on the seaward faces of the bars. We thus define the inner surf zone for $x < 340$ m and the outer surf zone for $340 \le x < 500$ m. The wave amplitude decreases toward the shore in a stepwise manner corresponding to the occurrences of wave breaking. The wave period and direction are slightly modulated within the inner surf zone, while the waves propagate westward approximately normal to the shore ($|\theta_p| < 0.16°$). Likewise, the resultant mean barotropic Eulerian offshore velocity u_{bt}, whose time average is approximately anti-Stokes (cf. UMR09) because the steady cross-shore mass balance requires the anti-Stokes profile, $\partial_x u_{bt}^l = 0$, where $u_{bt}^{St} < 0$. The small deviation from the normal direction in θ_p invokes the weak time-averaged northward current of $v_{bt} < 0.11$ m/s for the 3-D case, whereas $v_{bt} < 0.05$ m/s with the seaward peak shift by 30–40 m manifests in the 2-D model. The associated v_{bt}^{St} is negligibly small with $|v_{bt}^{St}| < 1$ mm/s. The quantitative consistency in the rip currents (u_{bt}) and the perpendicular component (v_{bt}) ensures that the 3-D and 2-D models represent the equivalent results of transient rip currents, which allow us feasible inter-model comparisons.

3.2. 3-D Structures

Instantaneous 3-D flow fields of unstable, transient rip currents at $t = 299$ and 327 min are depicted with the near-surface and near-bed velocity vectors on the associated barotropic relative vorticity (Figure 3). Snapshots of the 8 cross-sectional distributions of 3-D velocity at $t = 299$ min are plotted in Figure 4. At $t = 299$ min, the rip current bifurcates beyond the inner surf zone by $x = 340$ m, and the eruption of a mushroom-like, coherent vortex dipole with paired positive and negative vorticity is evident. In turn, finer vortices and elongated filaments dominate at $t = 327$ min, with strong vorticity aligning alongshore with a sign change at intervals of about 60–80 m near the shore ($x < 160$ m) that feeds initial development of rip currents. The torque of the breaker acceleration (see also section 4.2) yields positive and negative relative vorticity in the surf zone, leading to alternate offshore and onshore currents aligned in the alongshore direction that can readily be unstable [e.g., *Haller and Dalrymple*, 2001; *Yu*, 2006]. The developed rip cells at $t = 299$ min are not quite persistent with time, but short-lived particularly in the 3-D model. The coherent eddies subsequently collapse into much finer vortices and elongated filaments such as those at $t = 327$ min, followed by reorganization to evolve into coherent eddies and perceptible rip currents (not shown). This process occurs quasi-periodically at a period of *O* (1–10) min, which fits the VLF band (section 3.4).

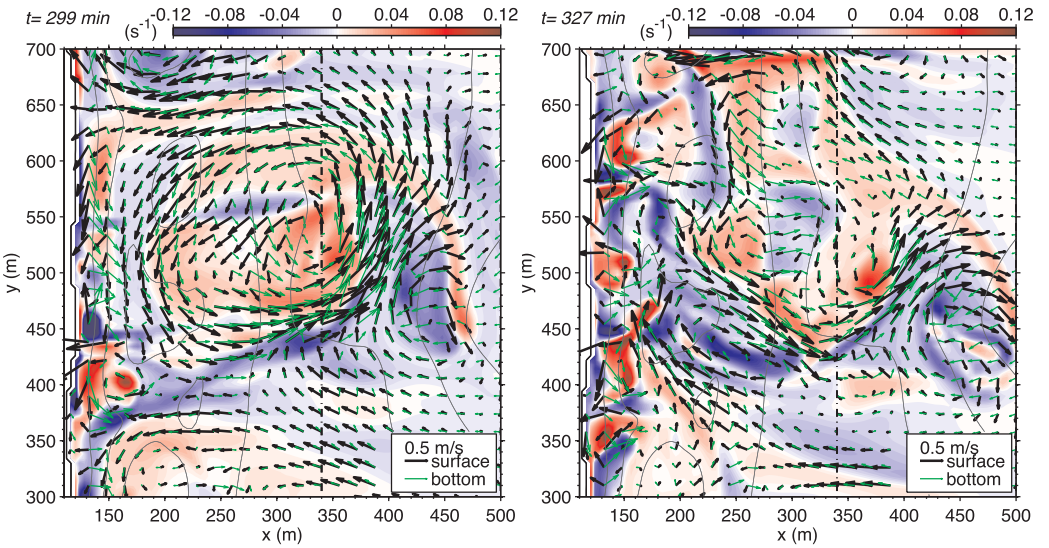

Figure 3. Plan view plots of instantaneous 3-D rip cells in the blow-up region shown in Figure 1 at (left) (a) $t = 299$ and (b) (right) 327 min after the initialization. The near-surface, top-most s-layer horizontal velocity (black) and the near-bed, bottom-most s-layer horizontal velocity (green) and the barotropic relative vorticity (color) are depicted. The vertical dashed lines denote the approximate offshore extents of the inner surf zone ($x < 340$ m). The thin contours are isobaths at 1 m intervals. At $t = 299$ min, eruption of a mushroom-like, coherent vortex dipole with paired positive and negative vorticity is evident, while finer vortices and elongated filaments dominate at $t = 327$ min. The velocity vectors are subsampled every 4 grid-points.

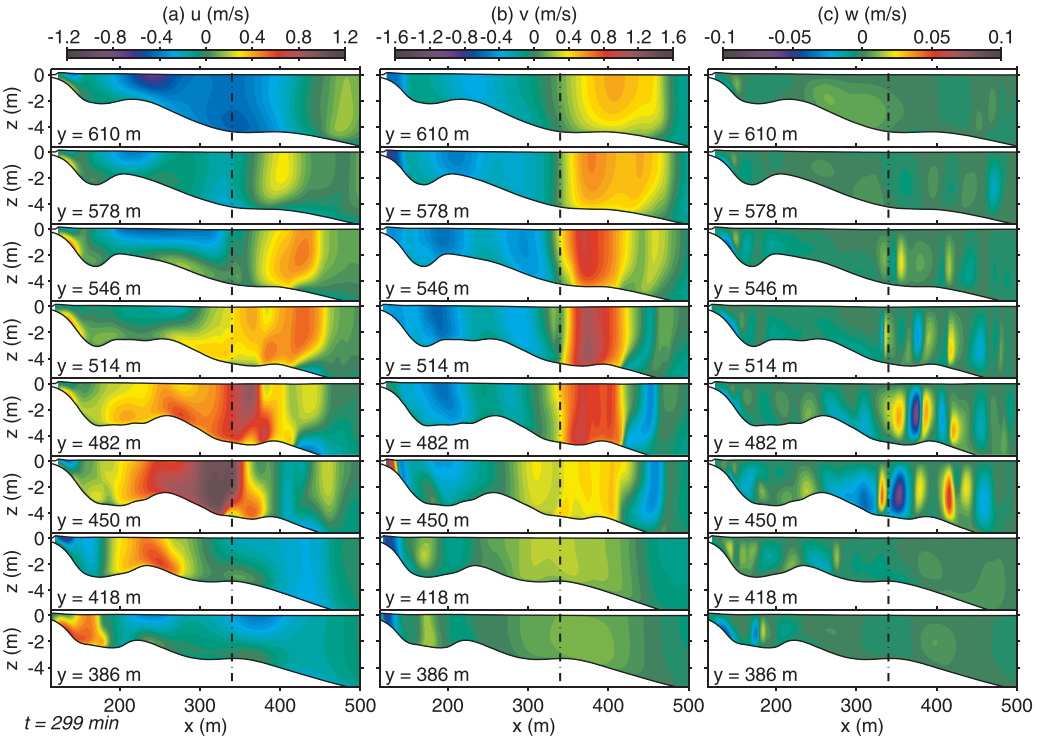

Figure 4. Snapshots of the 3-D structure of rip currents at $t = 299$ min (see Figure 3a for the plan view). (left) Offshore velocity u, (middle) northward alongshore velocity v, and (right) vertical upward velocity w are plotted along 8 alongshore cross-sections at 32 m intervals in y. The vertical dashed lines denote the approximate offshore extents of the inner surf zone ($x < 340$ m). The main offshore rip current is developed around $y = 450$–482 m with the peak u at 1–3 m depths along with strong up- and down-welling w up to ± 10 cm/s indicating prominent convergence and divergence.

Vigorous offshore eruption of the rip current is demonstrated at $t = 299$ min around the rip channel formed near $y = 460$ m (Figure 1). It gradually veers northward, followed by a further left turn, resulting in a laterally circulating cyclonic rip cell with a diameter of about 250 m. The seaward rip current velocity extends up to $x = 450$ m, about 1.7 times as wide as the surf zone width. Affected by the near-surface breaker-driven flow and the near-bed undertow, the maxima of the offshore-directed rip current in u appear at depth, typically at 1–3 m below the mean sea surface, rather than right at the surface. In contrast, the onshore return flow ($u < 0$) has a surface confined structure (Figure 4a: $514 \leq y \leq 610$ m, $x < 300$ m) due to the coincident onshore breaker acceleration near the surface. Depth-dependency is more pronounced both in u and v especially where velocity magnitude is small, while the main body of the rip current has less prominent vertical structure (Figure 3). Associated vertical velocity w reaches several cm/s particularly near the main rip. At $y = 450$, 482 and 514 m in Figure 4c, upwelling occurs on the both sides of the main rip, whereas downward flow is formed at the rip center where vertical vorticity changes its sign (Figure 3). These results indicate that the 3-D rip currents are composed of pairs of the counter-rotating longitudinal (i.e., following the rip current) overturning roll cells that lead to convergence of the surface flow at the rip center while divergence at the bottom.

3.3. Spatiotemporal Development

The 3-D transient rip currents are compared with the 2-D counterpart. Figure 5 shows sequential blow-up snapshots of the barotropic relative vorticity $\boldsymbol{q} = \nabla_H \times \mathbf{u}_{bt}$ for $290 \leq t \leq 330$ min at 10 min intervals from the 2-D and 3-D models. Time-varying transient rip currents and associated vortices are evident with the quasi-persistent strong rip current formed in the rip channel around $y = 460$ m. In addition, offshore eruption of rip currents occurs at other places, including those originating from the shore at around $y = 250$, 650 and 750 m. The approximate maximum offshore extent of the rip currents is slightly beyond $y = 500$ m. The 2-D model clearly illustrates more organized, coherent vortices that roll up into circular-shaped eddies to form positive and negative vortex dipoles. By contrast, such organized structures are immediately destroyed in the 3-D model. The 3-D rip-induced vortices tend to be stretched seaward and to evolve into filaments and streaks. As a consequence, the horizontal aspect ratio of the 3-D vortices is distorted with longer cross-shore length scales as compared to the 2-D case.

3.4. Intrinsic VLFs

The rip currents for the surveyed bathymetry under the near-normal incident steady waves are intrinsically unstable with low frequency variability (Figure 5). We define the four sampling stations, Sta. A–D (Figure 1),

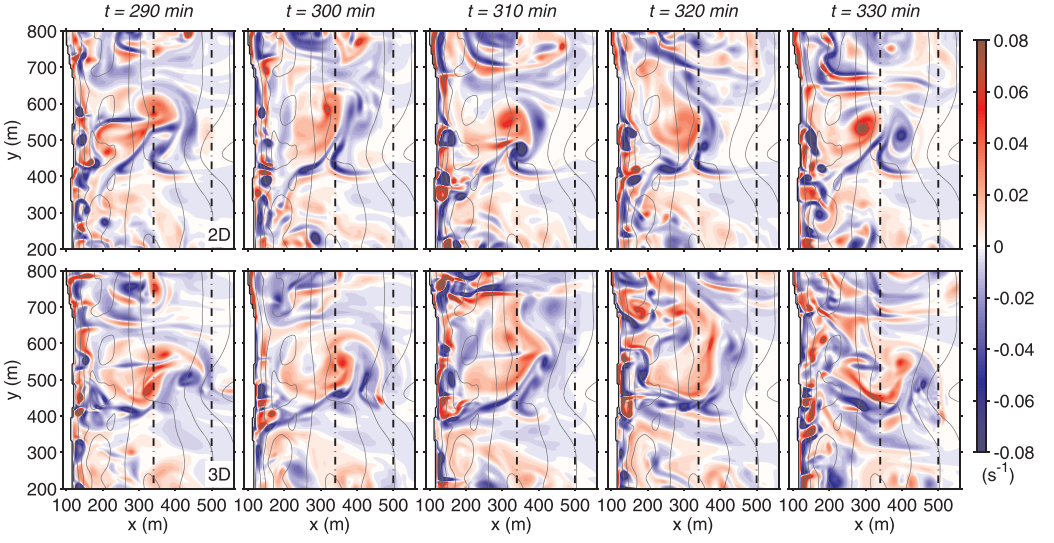

Figure 5. Temporal evolution of the barotropic relative vorticity $q = \nabla_H \times \mathbf{u}_{bt}$ in color for the 2-D (top row) and 3-D (bottom row) cases at 10-minute intervals. The two vertical dashed lines denote the approximate offshore extents of the inner ($x < 340$ m) and outer ($340 \leq x < 500$ m) surf zones. The thin contours are isobaths at 1 m intervals. The main rip is formed and fluctuates in the middle of the domain with a pair of counter-rotating vortex dipole. This structure tends to roll up into circular shapes in the 2-D particularly at $t = 310$ and 330 min, while the 3-D vortex pair is more stretched longitudinally and elongated as filaments.

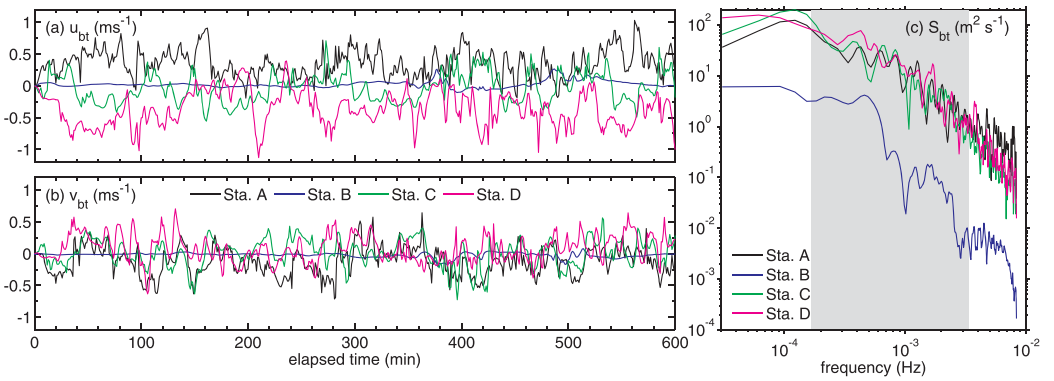

Figure 6. Time series of (a) cross-shore barotropic velocity u_{bt}, (b) alongshore barotropic velocity v_{bt}, and (c) frequency power spectra of the barotropic kinetic energy, S_{bt}, from the fully 3-D model, at the 4 sampling stations (Figure 1) chosen for the prevailing seaward rip current (Sta. A), the offshore quiescent rip current (Sta. B), the bifurcation on the shoal (Sta. C), and the shoreward return flow (Sta. D). The shaded area in Figure 6c represents the VLF band for the periods between 5 and 100 min.

to monitor temporal fluctuations of the transient rip currents and their frequency spectra. The choice is made intentionally for the prevailing seaward rip current (Sta. A), the offshore quiescent rip current (Sta. B), the bifurcation on the shoal (Sta. C), and the shoreward return flow (Sta. D). The barotropic velocity time series plots (Figures 6a and 6b) clarify that the rip current, the return flow, and the bifurcating flow fluctuate with time and are composed of many frequency components as depicted in their kinetic energy frequency spectra (Figure 6c). The predominant fluctuations occur for the periods of 30–80 min with higher frequency variability superposed. The higher frequency components are significantly weak at the offshore Sta. B, whereas the lower frequency energy is still apparent. The energy is extensively distributed in broadband and thus the spectra are "red" to some extent, which may require more elaborate methods such as with frequency-wavenumber spectra to selectively extract the vortical component of the VLFs from that irrotational part involving infragravity waves [e.g., *MacMahan et al.*, 2010b; *Feddersen*, 2014]. Nevertheless, with a visual guide from Figures 6a and 6b, spectral peaks are detected at about 5×10^{-4} Hz (33.3 min) and 2×10^{-3} Hz (8.3 min) at all the 4 stations (Figure 6c), fitting the VLF band of $f < 0.004$ Hz [e.g., *Reniers et al.*, 2007]. Therefore, we define our VLF band for the periods between 5 and 100 min and extract the intrinsic VLF variability from the model results using a frequency band-pass filter.

4. Intrinsic VLFs in 3-D Transient Rip Currents

4.1. Eddy Statistics

To extract 3-D effects on turbulent rip currents and associated vortices, we first examine cross-shore profiles of depth- and alongshore-averaged eddy statistics (Figure 7). For the 3-D case, we introduce decompositions into the depth-invariant barotropic component $\mathbf{u}'_{bt}$, the depth-dependent baroclinic component $\mathbf{u}'_{bc}$, and their sum as the total, where the prime and the subscrirpt *bc* respectively stand for the deviation from the ensemble (time) average denoted by the over bar, and the depth-dependent component (i.e., $\mathbf{u}=\overline{\mathbf{u}}+\mathbf{u}'$; $\mathbf{u}=\mathbf{u}_{bt}+\mathbf{u}_{bc}$). Based on these notations, the EKE $\left(=\left(\overline{u'^2}+\overline{v'^2}\right)/2\right)$ and kinematic lateral Reynolds stress $(=-\overline{u'v'})$ are decomposed into the barotropic component with $\mathbf{u}'_{bt}$ and the baroclinic component with $\mathbf{u}'_{bc}$ for the 3-D case. Furthermore, the barotropic EKE production rate, denoted by K_mK_e, in an EKE conservation equation is

$$K_mK_e = -\overline{u'^2_{bt}} \cdot \partial_x \overline{u_{bt}} - \overline{u'_{bt}v'_{bt}} \cdot \partial_y \overline{u_{bt}} - \overline{u'_{bt}v'_{bt}} \cdot \partial_x \overline{v_{bt}} - \overline{v'^2_{bt}} \cdot \partial_y \overline{v_{bt}}, \quad (1)$$

which accounts for the mean to eddy kinetic energy conversion rate responsible for feeding shear instability if it is positive.

In Figure 7a, the barotropic and total EKE of the 3-D model are approximately the same as the barotropic EKE of the 2-D model, although the 3-D EKEs are slightly larger. The baroclinic EKE contributes only 5.0% to the total EKE. The depth-averaged horizontal Reynolds stress (Figure 7b) shows the largest difference between the two models among the other statistics. The peak magnitudes appear near the shore

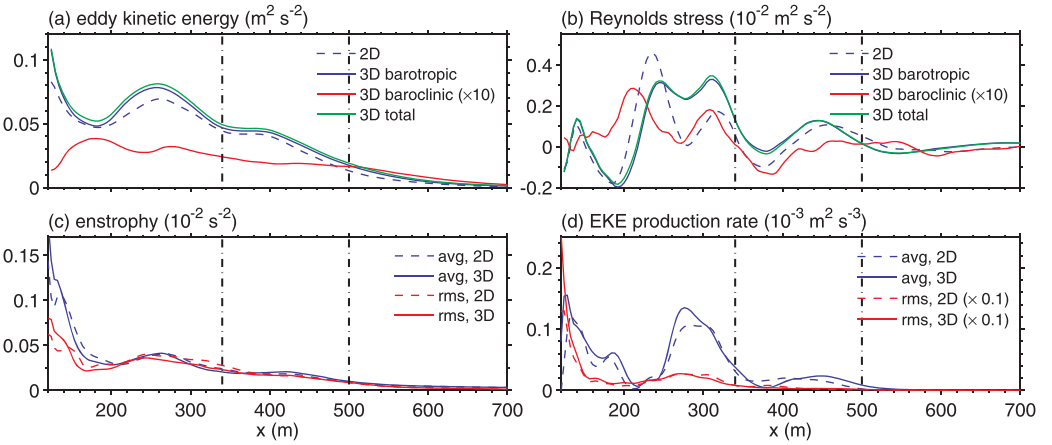

Figure 7. Cross-shore profiles of depth- and alongshore-averaged (a) eddy kinetic energy (EKE), (b) lateral kinematic Reynolds stress, (c) time-averaged enstrophy of barotropic vorticity ($q^2/2$), and (d) barotropic EKE production rate (equation (1)). The RMSs in Figures 7c and 7d are the deviations from the alongshore average. The two vertical dashed lines denote the approximate offshore extents of the inner ($x < 340$ m) and outer ($340 \leq x < 500$ m) surf zones.

($x = 140$ m) and shoreward of the inner bar ($x = 240$ m), both of which are close to the peaks of the breaker acceleration ϵ^b (Figure 2b) where the total EKE increases (Figure 7a). The third peak from the shore emerges further offshore at $x = 320$ m in both the models, whereas the 3-D Reynolds stress is more widely distributed in x with the baroclinic contribution having 6.2% of the total. The time- and alongshore-averaged enstrophy of the barotropic vorticity q significantly increases near the shore (*feeder* region; $x < 200$ m) in the 3-D case (Figure 7c), consistent with the barotropic EKE (Figure 7a), while their cross-shore averages for $x \leq 600$ m are almost identical. In Figure 7d, the alongshore-averaged $K_m K_e$ is always positive with the 3 peaks approximately coinciding with those of ϵ^b and EKE, which evidently demonstrates that shear instability intensifies EKE as the major source of transient rip currents [e.g., *Haller and Dalrymple*, 2001] in particular in the *feeder* region and the inner surf zone ($x < 340$ m). The 3-D $K_m K_e$ is somewhat larger than that of the 2-D, consistent with the EKE. The difference is greatest around the peaks, in particular in the vicinity of the shore ($x < 140$ m) and the inner bar crest ($x \approx 270$ m). In summary, the 3-D model enhances overall eddy activity in transient rip currents due to the increased production rate around the breaking points, particularly on the sloping shore face and the inner bar crest. The former accentuates enstrophy significantly right at the shore, while the latter correlates with modification in the cross-shore profile of the horizontal Reynolds stress with enhanced $K_m K_e$, leading to more pronounced shear instability. Nevertheless, the depth-dependent transient velocity $\mathbf{u}'_{bc}$ makes moderate contributions, by about 5–6%, to the generation of the EKE and the Reynolds stress.

4.2. Barotropic Vorticity Budget

The conservation equation for the barotropic vorticity $q = \nabla_H \times \mathbf{u}_{bt}$ is derived by taking the curl of the barotropic momentum equation in equation (A5).

$$\partial_t q + \underbrace{\nabla_H \times [(q+f_c)\hat{\mathbf{z}} \times \mathbf{u}_{bt}]}_{\text{advection (adv)}} = -\nabla_H \times (f_c \hat{\mathbf{z}} \times \mathbf{u}_{bt}^{St}) \underbrace{-\nabla_H \times (q\hat{\mathbf{z}} \times \mathbf{u}_{bt}^{St})}_{\text{curl J}} + \underbrace{\nabla_H \times \frac{\boldsymbol{\tau}_{sur}}{\rho_0 D}}_{\text{curl B}} \underbrace{-\nabla_H \times \left(\frac{\in^{wd}}{\rho_0 \sigma D} \mathbf{k} \right)}_{\text{curl S}} \underbrace{-\nabla_H \times \frac{\boldsymbol{\tau}_{bot}^{cd}}{\rho_0 D}}_{\text{curl D}} \tag{2}$$

Notice that the left hand side (LHS) terms are the nonwave contributions comprising the tendency and advection effects combined with vorticity stretching (adv), while all the right hand side (RHS) terms reflect WEC. Because we assume no rotation with $f_c = 0$, the Stokes-Coriolis (the first RHS) term vanishes. The other RHS terms are the vortex force torque (curl **J**), the breaker acceleration torque (curl **B**), the bottom boundary streaming torque (curl **S**), and the bottom drag torque (curl **D**). Such barotropic vorticity analyses have been conducted in *Bonneton et al.* [2010] and *Bruneau et al.* [2011] with 2-D models based on a wave-averaged shallow water equation considering the vortex force [*Smith*, 2006; *Ardhuin et al.*, 2008]. Both concluded that the curl **B** is the main source of vorticity, yet the curl **J** was not discussed and curl **S** was omitted.

Figure 8 shows snapshots of the barotropic vorticity q, the Lagrangian transport $D\mathbf{u}_{bt}^{l}$, the RMS wave height H_{rms}, the vorticity advection term (adv), and the four WEC torques for the 3-D case at $t = 300$ min when the energetic rip current and the associated counterclockwise rotating transport develop on the rip channel around $y = 460$ m. The advection is the leading term that approximately balances with the sum of the tendency term (not shown) and the four RHS WEC terms. In the *feeder* region for $x < 200$ m, q is forced by the intense curl **B**, where wave breaking occurs as partially depicted by shoreward decreasing H_{rms}, but compensated for by the curl **D**. Thus, alongshore-varying vorticity sources for the intrinsic VLFs are generated with the strong bathymetric constraint as argued in *Geiman and Kirby* [2013]. Note that random directional incident waves lead to finite breaking crest-length vorticity generation, which also provokes alongshore-variable q source for the forced VLF excitation [*Spydell and Feddersen*, 2009]. In the large portion of the offshore area ($x > 200$ m), the curl **D** substantially absorbs q as exhibited by the similar spatial distribution with the opposite sign. In the *neck* region ($200 < x < 340$ m), q is fed again by curl **B** where the EKE production rate is considerably intensified (Figure 7d). The curl **S** resembles the curl **B** in the patterns and is generally negative to decelerate offshore-directed flow including rip currents, while the curl **S** is much smaller than the curl **B** by only a few percent.

The vortex force torque curl **J** plays a dominant role in the vorticity budget other than the breaker torque curl **B** as the primary vorticity source. The contribution of curl **J** reaches about 60–70% of curl **B**, which is quite significant. In the 2-D momentum balance, the vortex force is known to counteract the breaker acceleration [*Bruneau et al*., 2011]. To examine the role played by the vortex force in the 2-D vorticity balance, we further rearrange curl **J** into:

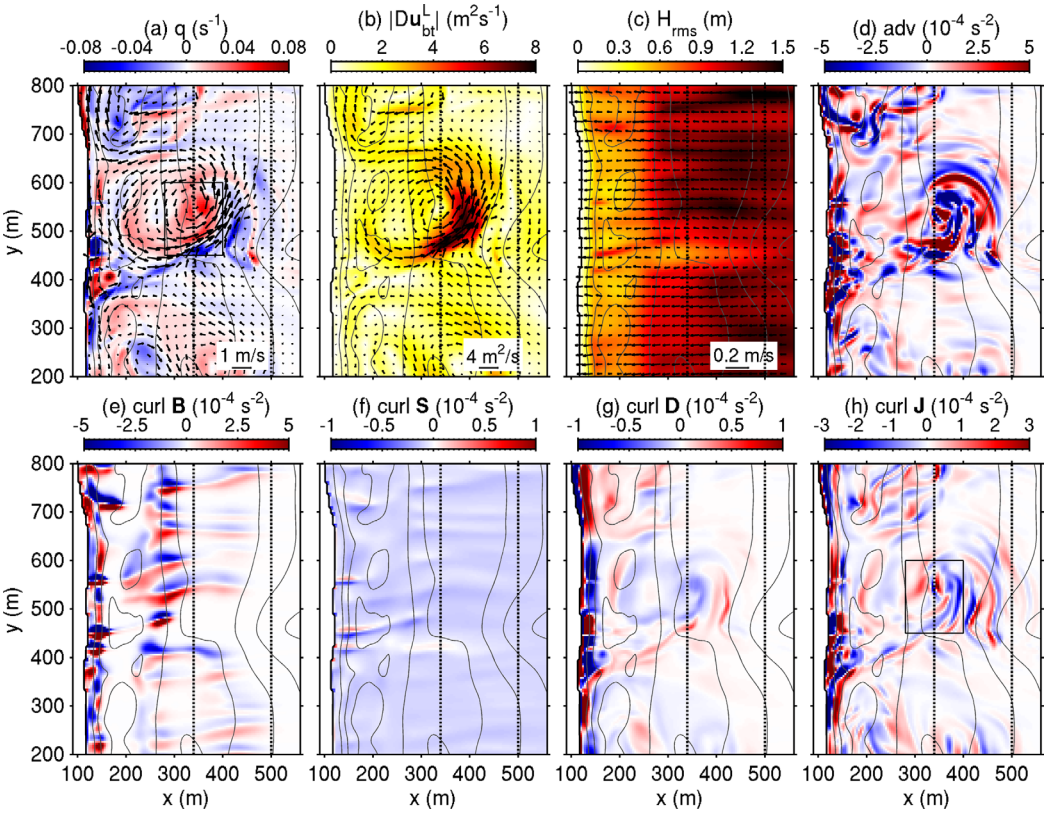

Figure 8. Snapshots of (a) barotropic vertical vorticity q (color) and the barotropic velocity $\mathbf{u}_{bt}$ (vectors), (b) Lagrangian transport $D\mathbf{u}_{bt}^{l}$ (vectors) and its magnitude (color), (c) RMS wave height and barotropic Stokes drift $\mathbf{u}_{bt}^{St}$ (vectors), (d) vorticity advection term, (e) breaker acceleration torque curl **B**, (f) bottom-streaming torque curl **S**, (g) bottom drag torque curl **D**, and (h) vortex force torque curl **J**, at $t = 300$ min for the 3-D case. Notice that different color scales are used. The two vertical dashed lines denote the approximate offshore extents of the inner ($x < 340$ m) and outer ($340 \le x < 500$ m) surf zones. The thin contours are isobaths at 1 m intervals. The main rip vorticity and associated offshore Lagrangian transport appear around the middle of the domain, forced by the curl **B** that determines the initial width of the rip jet near the shore (*i.e.*, the *feeder* region). Nevertheless, the vortex dipole develops with longer alongshore wavelength in and beyond the *feeder* region ($200 < x < 340$ m; the *neck* region) where the predominant torque is curl **J**, while curl **D** is secondarily important. In contrast, curl **S** is generally negative to decelerate the offshore-headed flow but is much less than the other torques by an order of magnitude. Note that the 2D vorticity balance is qualitatively the same and thus is not shown.

$$\text{curl } \mathbf{J} = -\nabla_H \times \left[q\hat{\mathbf{z}} \times \mathbf{u}_{bt}^{St}\right] = -\nabla_H \cdot \left(\mathbf{u}_{bt}^{St} q\right) = -\left[\partial_x\left(u_{bt}^{St} q\right) + \partial_y\left(v_{bt}^{St} q\right)\right]. \quad (3)$$

Because $\theta_p \approx 0$ (Figure 2b) and $v_{bt}^{St} \approx 0$ (Figure 2d), curl $\mathbf{J} \approx -\partial_x\left(u_{bt}^{St}\eta\right)$. On the present coordinate system, u_{bt}^{St} generally increases from the shore except for the decreasing regions shoreward of the breaking points near the two longshore bars (Figure 2c). In regions of the seaward increasing u_{bt}^{St}, positive (negative) q results in negative (positive) curl **J**, and thus q always reduces its magnitude. The opposite is true where u_{bt}^{St} decreases seaward. Consequently, the rip currents and associated vorticity are extensively suppressed under the near-normal onshore u_{bt}^{St} condition, whereas they recharge vorticity in the shoreward of the breaking points before going out to the offshore *rip-head* region ($340 < x < 500$ m; the outer surf zone). For instance, the positive q of the main rip eddy indicated by the black boxes in Figures 8a, h is increased by the positive curl **J** in the shoreward of $x = 340$ m, whereas decreased by the negative curl **J** beyond that.

Therefore, in the transient rip currents, the four wave-induced forcing terms substantially modify the usual nonwave vorticity balance. The breaker torque (curl **B**) is the primary vorticity source particularly in the *feeder* region near the shore and is generally reduced by the bottom drag torque (curl **D**) and the bottom streaming torque (curl **S**). The vortex force torque (curl **J**) has magnitudes comparable to curl **B** and works not only as an overall vorticity sink, but also as a source in the shoreward of the breaking points, where u_{bt}^{St} decreases offshore, coincidently with curl **B**. In the *rip-head* region ($x > 340$ m), as the curl **B** almost vanishes, the nonwave advection term takes over the vorticity balance to compete with the tendency term. Note that the barotropic vorticity budget of the 2-D case is qualitatively the same as the 3-D case, and thus is not shown here. In addition, the above argument is most striking under conditions of strong rip currents, although the temporal RMSs of the terms provide less pronounced curl **J** effects reduced by 44–71% of those in Figure 8.

4.3. CEW and Three-Dimensionality on Intrinsic VLFs

In previous studies, attention has not been paid to influences of CEW and three-dimensionality on transient processes in the VLF band defined in section 3.4. Because CEW has been well known to reduce the offshore extent of the rip currents [*Haas et al.*, 2003; *Yu and Slinn*, 2003; *Weir et al.*, 2011], we further conduct two more simulations using the same 3-D and 2-D models without CEW (denoted by NC). Figure 9 shows the cross-shore profiles of the time- and alongshore-averaged total kinetic energy KE_{bt}, EKE for the VLF band EKE_{vlf}, the ratio of EKE_{vlf} to the total EKE (EKE_{tot}), and a mean VLF period T_{m2} for the 4 cases. The last item is evaluated as the square-root of the ratio of two spectral moments,

$$T_{m2} = \sqrt{m_0/m_2}, \quad \text{where } m_n = \int_{-\infty}^{\infty} f_{bt}^n S_{bt}(f_{bt}) df_{bt} \quad (4)$$

f_{bt}: frequencies of the 2-D transient rip currents, and S_{bt} (f_{bt}): the barotropic kinetic energy frequency spectrum. The volume averages of the quantities in Figure 9 for $x \leq 600$ m are summarized in Table 2. Note that the barotropic velocity $\mathbf{u}_{bt}$ is exploited in the present analysis.

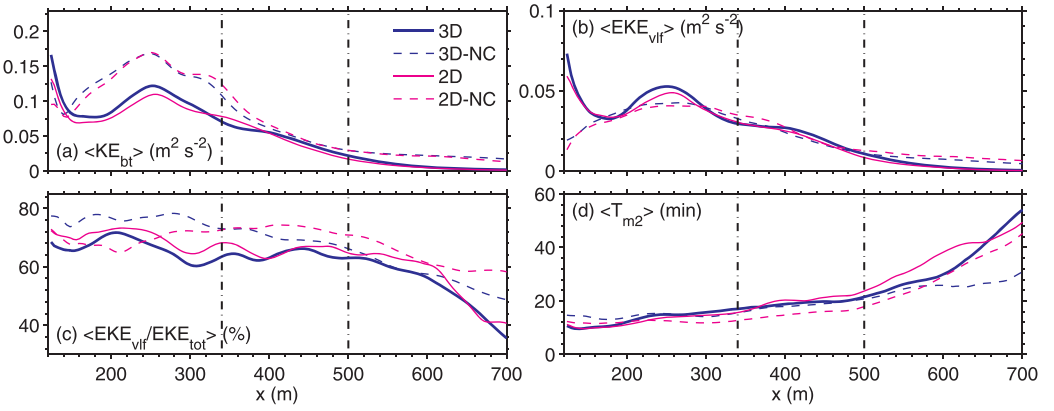

Figure 9. Cross-shore profiles of time- and alongshore-averaged (a) total barotropic kinetic energy KE_{bt}, (b) barotropic eddy kinetic energy in the VLF band EKE_{vlf}, (c) ratios of EKE_{vlf}/EKE_{tot}, where EKE_{tot} is the total barotropic EKE, and (d) the spectral mean VLF period T_{m2}, plotted for the 3-D (blue) and 2-D (magenta) cases. "NC" denotes the cases without CEW (broken curves). The two vertical dashed lines denote the approximate offshore extents of the inner ($x < 340$ m) and outer ($340 \leq x < 500$ m) surf zones. Differences are evident in KE_{bt} and EKE_{vlf} between the cases with CEW and the NC cases.

Table 2. Volume-Averages of the Variables Plotted in Figure 9 Averaged for $x \leq 600$ m

	3-D	3D-NC	2-D	2D-NC	Unit
KE_{bt}	6.25	8.49	5.75	8.54	10^{-2} m^{2}s^{-2}
EKE_{tot}	4.28	3.45	3.83	3.67	10^{-2} m^{2}s^{-2}
EKE_{vlf}	2.80	2.53	2.62	2.58	10^{-2} m^{2}s^{-2}
T_{m2}	17.9	17.7	18.9	15.4	min
EKE_{tot}/KE_{bt}	71.9	46.1	69.5	49.2	%
EKE_{vlf}/KE_{bt}	46.1	32.2	46.5	34.4	%
EKE_{vlf}/EKE_{tot}	64.3	71.1	67.1	70.1	%

The 2-D and 3-D differences are subtle as expected for our choice of the bottom drag parameterization (Appendix C). The inclusion of CEW prominently alters not only $<KE_{bt}>$, but also $<EKE_{vlf}>$. As the effect of reducing the offshore extent of the rip current, $<KE_{bt}>$ decreases remarkably due to CEW in the *neck* and *rip-head* regions (i.e., $160 < x < 350$ m) where the rip currents are most active (e.g., Figure 8). The overall reduction of KE_{bt} due to CEW reaches 26–33%. However, intensification of $<EKE_{vlf}>$ is caused by the CEW with the most influential region in the vicinity of the shore (i.e., the *feeder* region). In addition, CEW enhances $<EKE_{vlf}>$ around $x = 260$ m, where intensive depth-induced breaking occurs with the large ϵ^b (Figure 2b). The $<EKE_{tot}>$ profiles are more or less similar to those of $<EKE_{vlf}>$ (not shown). Thus, the EKE_{vlf} to EKE_{tot} ratios are mostly unaltered in x with the modest seaward decreasing trend in the offshore region ($x > 500$ m), where rip currents barely reach. The EKE_{vlf} to EKE_{tot} ratio ranges from 64.3 to 71.1% with a moderate decrease by the CEW. The mean fluctuation period T_{m2} monotonically increases seaward with the spatial averages ranging from 15.4 to 18.9 min, thus the predominant variability is in the VLF band. In contrast, the EKE_{vlf} to KE_{bt} ratio considerably increases from 32.2 and 34.3% without CEW (NC) to 46.1 and 46.5% with CEW.

The above result manifests that CEW intensifies overall variability as well as that in the VLF band in the transient rip currents on the realistic bathymetry either with the 3-D or 2-D model. Furthermore, the impact of CEW on EKE_{vlf} emerges as a modification of the cross-shore profile of EKE_{vlf}. The intensification by CEW is most evident where ϵ^b is magnified. As argued in UMR09, in the barotropic shear waves on an idealized bathymetry, CEW decelerate the intrinsic VLFs associated with shear waves due to the wave ray bending and the resultant magnification of the shoreward breaker momentum that counteracts with the seaward momentum transport of the background alongshore currents. The plausible underlying mechanism for the transient rip currents is that the shoreward contraction effect due to CEW [cf. *Yu and Slinn*, 2003] hinders seaward transport of EKE to accumulate EKE within the surf zone (Figure 9b). Several other mechanisms are possible causes of the difference from the shear wave case. For instance, the broadband nature of the turbulent rip currents generated on the complex, realistic bathymetry (Figure 6) may alter the CEW responses because waves *feel* current fluctuations comparable to or greater than their own wavelength according to the ray theory. Alignments of the principal direction of the background rip currents and incoming waves may provoke their mutual interaction through the vortex force that can lead to the vorticity reduction and magnification in the *neck* region (section 4.2).

4.4. Bathymetric Variability on Intrinsic VLFs

In literature, intrinsically unstable rip currents have hardly been explicit in the modeling studies on relatively simplified bathymetries forced by steady, uniform incident waves [e.g., *Yu and Slinn*, 2003; *Weir et al*., 2011; *Kumar et al*., 2012], except for *Geiman and Kirby* [2013] as argued in section 4.2. In this subsection, a quantitative assessment is performed to examine influences of the bathymetric variability on the intrinsic VLFs. A set of synthetic bathymetries is introduced based on the surveyed bottom profile $h(x,\ y)$ as depicted in Figure 1. We define a parameter α that controls the alongshore variability in the following form:

$$h(x,y) = \langle h \rangle(x) + \alpha h'(x,y); h'(x,y) = h(x,y) - \langle h \rangle(x), \tag{5}$$

where $\langle h \rangle(x)$: the alongshore-averaged bed profile, and $h'(x,y)$: the perturbation relative to $\langle h \rangle(x)$. The original, surveyed profile is retrieved with $\alpha = 1$, while the alongshore-uniformity is achieved by $\alpha = 0$. We carry out the full 3-D simulations with CEW for $\alpha = 0$, 0.01, 0.1, 0.2, 0.5, 1, 1.2, and 1.5. Note that the sea bed partially pokes out to the sea surface during the simulations when $\alpha \geq 1.7$. The other conditions, including the offshore incident waves, are unchanged as configured in the previous sections. This α parameter is contexturized with the following bulk metric that measures alogshore bathymetric nonuniformity:

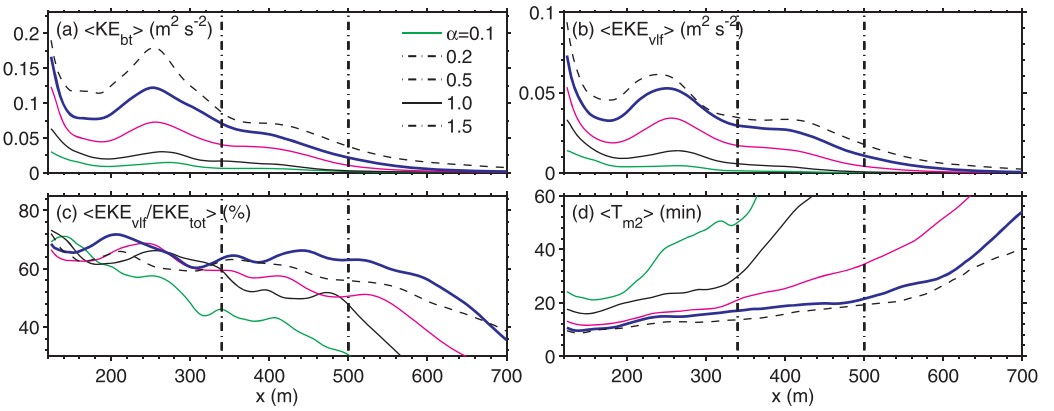

Figure 10. Same as Figure 9, but for the 3-D runs with CEW on several bed profiles, controlled by the perturbation parameter, α (equation (5)). Proportionality to α is pronounced in KE_{bt}, EKE_{vlf}, and EKE_{vlf}/EKE_{tot} although T_{m2} are inversely proportional to α.

$$\chi^2 = \frac{1}{L_x L_y}\int_0^{L_x}\int_0^{L_y}\left[\frac{h(x,y)-\langle h\rangle(x)}{\langle h\rangle(x)}\right]^2 dy\ dx, \tag{6}$$

where L_x and L_y are the cross-shore and alongshore lengths of the domain. For the Duck beach, *Ruessink et al.* [2001] and *Feddersen and Guza* [2003] reported χ^2 ranges 0.002–0.021 with the average of 0.0038 ± 0.008. Our original bathymetry (α=1) gives us χ^2=0.01346, from which we can evaluate $\chi^2 = 0.01346 \cdot \alpha^2$ for any α. Thus, $\alpha \approx 0.53$ corresponds to the averaged Duck condition, while $\alpha = 1$ fits the typical nonumiform regime that has frequently been observed.

Propotionality to α is manifested in the crosshore profiles of $<KE_{bt}>$ (Figure 10a) and $<EKE_{vlf}>$ (Figure 10b). They both are positively correlated with α (Figures 11a and 11b) and well approximated by cubic polynomials while retaining the similarity in the cross-shore profiles. Unless α is too small (*viz.*, $\alpha \leq 0.1$), the ratios of $\ll EKE_{vlf}/EKE_{tot}\gg$ are about 60% on average (Figure 11c) and do not vary that much with moderate shoreward amplifications with increased α (Figure 10c). Similarly, the ratios of $\ll EKE_{vlf}\gg$ to $\ll KE_{bt}\gg$ are about 40%. Note that $\alpha = 0$ does not generate any rip currents and merely is in the steady cross-shore momentum balance between the breaker acceleration and the pressure gradient force associated with wave set-up $g\partial_x \zeta \approx \tau^x_{sur}/(\rho_0 D) = \epsilon^b k_x/(\rho_0 \sigma D)$ and the cross-shore anti-Stokes mass balance, $\partial_x u^l_{bt} = 0$ (cf. UMR09, UMS10) with $v_{bt} = 0$, leading to a negligibly small $<KE_{bt}>$ and zero EKEs.

In contrast, the spectral mean intrinsic VLF period $<T_{m2}>$ is inversely proportional to α with a seaward increasing trend (Figure 10d), ranging from 13 to 36 min on average (Figure 11d). The linear stability analysis of *Haller and Dalrymple* [2001] indicates the transient rip currents are viewed as the classical Bickely jet [e.g., *Marchesiello et al.*, 2015]. The corresponding oscillation frequency f_{HD} may be determined by the wavenumber $k_* = 0.639$ and frequency $\sigma_* = 0.255$ for the fastest growing sinuous mode as:

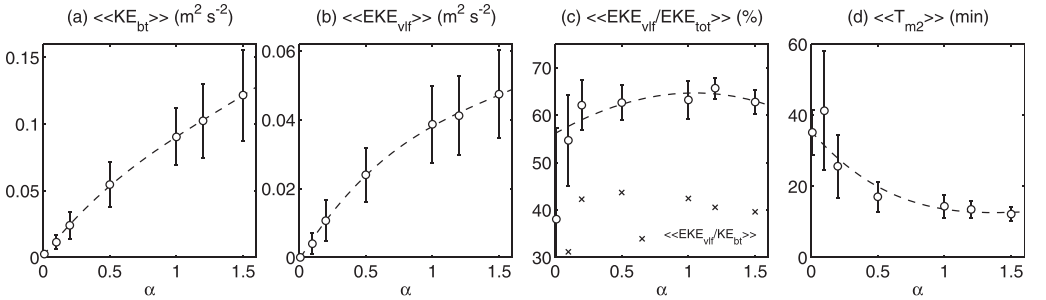

Figure 11. Scatter plots of the time- and volume-average (denoted by $\ll\cdot\gg$) of (a) KE_{bt}, (b) EKE_{vlf}, (c) EKE_{vlf}/EKE_{tot}, and (d) T_{m2} as functions of α (open circles) with the estimated cubic polynomial regressions (dashed curves) and the error bars. The ratios of $\ll EKE_{vlf}/KE_{bt}\gg$ are superposed with cross marks in Figure 11c. The cross-shore averages are taken for $x \leq 400$ m.

$$f_{HD} = \frac{\sigma_*}{2\pi}\frac{2U}{d} \approx 0.081 \cdot \frac{U}{d}, \tag{7}$$

where d: width of the jet, and U: jet velocity. In addition, a universal Strouhal number $S_t = f_B d/U \approx 0.181$ [*Bearman*, 1967] may alternatively be diagnosed because it is known to explain well the oscillating frequency f_B due to wakes and shear turbulence even in geophysical fluid for a wide range of Reynolds number. If we assume $d = 50$–200 m from the alongshore bathymetric variability (Figure 1) and jet widths (Figures 3 and 5) and $U = 0.2$–0.8 m/s (Figure 6), then f_{HD} gives the period of 13–204 min, while f_B gives 5–92 min. Although the latter agrees moderately better with the model result, both the frequency estimates suggest that the transient rip currents and their intrinsic VLFs are initiated by shear instability (see also section 4.1; Figure 7) and developed as shear turbulence. Consistent with Figure 10d, f_{HD} and f_B exhibit that the oscillation period becomes longer as U decreases, which is the case for the seaward decaying rip currents and for the attenuated $\ll KE_{bt} \gg$ due to the decreased bathymetric perturbation, α (Figure 11a). Therefore, bathymetric variability inherent in nature is viewed as essential to the onset and maintenance of the intrinsic VLFs in the transient rip currents even under time-independent, alongshore-uniform incident offshore waves, while the group waves and/or random waves introduce additional turbulent motion as the forced VLFs. In particular, the alongshore variability is responsible for the intrinsic VLFs through segmentation of rip cells due to the distributed curl **B** field (section 4.2).

4.5. Steady Forcing Magnitude on Intrinsic VLFs

To examine responses of the intrinsic VLFs to forcing magnitudes, the 3-D model is run for several steady incident wave height H_{rms} ranging from 0.1 to 2 m at the offshore open boundary with the other conditions kept unaltered. In the inner surf zone ($x < 340$ m), $<KE_{bt}>$, $<EKE_{vlf}>$, and $<EKE_{vlf}/EKE_{tot}>$ are evidently proportional to H_{rms} for $H_{rms} < 1.2$ m, whereas they decrease for $H_{rms} > 1.2$ m but are enhanced in the offshore (Figures 12 and 13). This outcome is qualitatively consistent with the 2-D model results on much simpler rip-channeled beaches in *Yu and Slinn* [2003]. The transition of the intrinsic VLF response to the incident H_{rms} is related to the wave breaking around the inner bar crest at $x = 240$ m (Figure 2c) that hinders H_{rms} and ε^b/ρ to develop $<KE_{bt}>$ and $<EKE_{vlf}>$ in the inner surf zone for $H_{rms} > 1.2$ m. Instead, the offshore breaking on the seaward face of the outer bar at $x = 400$ m is invoked in the higher wave conditions, which eventually takes over the breaking on the inner bar for $H_{rms} = 2.0$ m. The breaking around the inner- and outer-bars and associated shoreward momentum are known to suppress the offshore momentum transport (e.g., UMR09), resulting in the reduced $\ll KE_{bt} \gg$ and $\ll EKE_{vlf} \gg$ for higher waves (Figure 13). As expected from the discussion in section 4.4, the mean intrinsic VLF period is inversely proportional to H_{rms} for smaller waves, while it is approximately constant at ~18 min for $H_{rms} > 0.8$ m (Figure 13d). Note that the intrinsic VLF responses to the incident waves are anticipated to moderately vary with a choice of the wave breaking and bottom drag parameterizations [e.g., *Yu and Slinn*, 2003; *Weir et al.*, 2011].

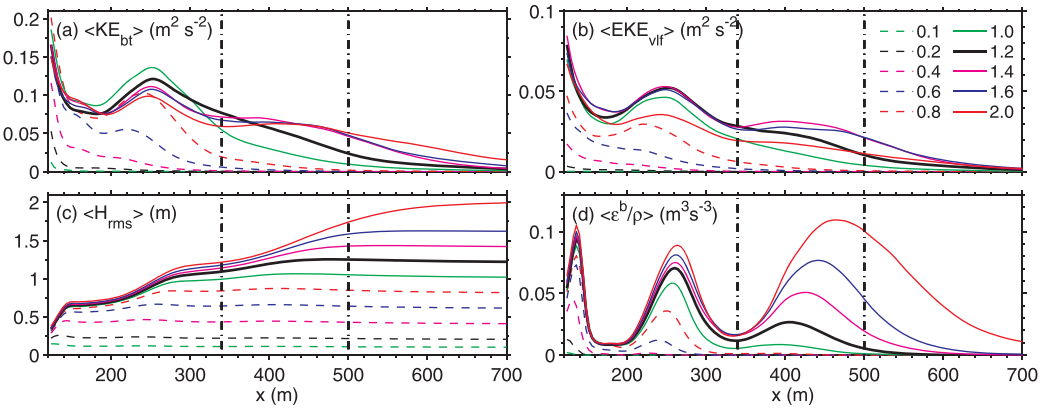

Figure 12. Cross-shore profiles of alongshore-averaged (a) total barotropic kinetic energy KE_{bt}, (b) barotropic eddy kinetic energy in the VLF band EKE_{vlf}, (c) RMS wave height H_{rms}, and (d) kinematic breaking acceleration ε^b/ρ for the 3-D CEW runs forced by the different incident H_{rms} in m indicated in the legend in Figure 12b. The two vertical dashed lines denote the approximate offshore extents of the inner ($x < 340$ m) and outer ($340 \le x < 500$ m) surf zones. KE_{bt} and EKE_{vlf} are proportional to H_{rms} for $H_{rms} < 1.2$ m, although the offshore breaking in Figure 12d predominates to rather suppress the VLFs in the surf zones.

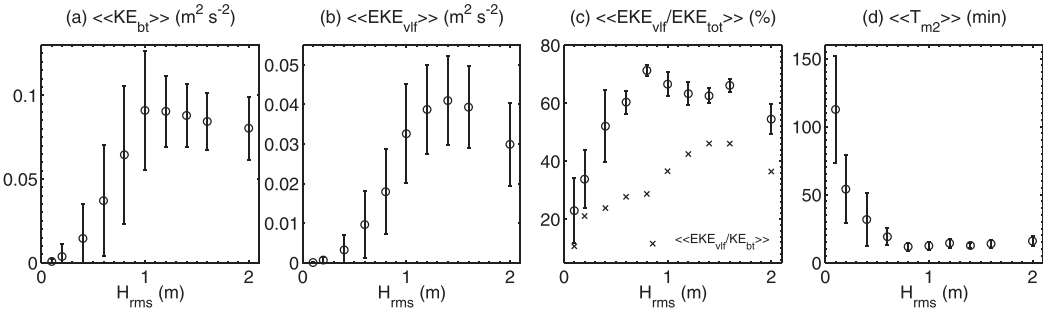

Figure 13. Same as Figure 11, but as a function of the imposed offshore incident wave height, H_{rms}.

Because the Duck bathymetry is known to be quite variable [e.g., *Lippmann and Holman*, 1990] due to morphodynamic processes primarily induced by waves and littoral currents, a qualitative comparison between the present model and the observation is a nontrivial task. In the present study, we take advantage of the estimation conducted by *MacMahan et al*. [2010b], who evaluated in situ VLFs on the same beach at Duck, NC, using the data set for 13–15 November 1997, during the *SandyDuck* field experiment. The energetic VLFs of rip currents were intentionally extracted by the conditional sampling for the offshore $H_{rms} > 0.5$ m and θ_p ranging between -9 and 13° to avoid strong alongshore currents. The VLFs are decomposed into the irrotational and rotational parts: the forced VLFs due to infragravity waves arising from group waves and the intrinsic VLFs relevant to the present study. The resultant intrinsic VLFs are proportional to H_{rms} with pronounced magnification in the surf zone. The estimated intrinsic EKE_{vlf} in the surf zone ranges 0.04–1.81 $\times$ 10^{-2} m^2s^{-2} for the local H_{rms} between 0.2 and 1.36 m, interpreted from equation (1) and Figure 4 of *MacMahan et al*. [2010b]. The forced VLFs due to infragravity waves were at the same magnitude as the intrinsic EKE_{vlf}. A quantitatively similar result was reported by *de Schipper et al*. [2012], who extended the analysis of *MacMahan et al*. [2010b] for the much longer period between August and December 1997. In turn, the ROMS-WEC model yields $<EKE_{vlf}>$ at about 2.5–2.8 $\times$ 10^{-2} m^2s^{-2} for $\alpha = 1$ and $H_{rms} = 1.2$ m (Table 2). Furthermore, $<EKE_{vlf}>$ broadly ranges between 1.89 $\times$ 10^{-3} -3.23 $\times$ 10^{-2} m^2s^{-2} for $H_{rms} = 0.4$–1.4 m (Figure 13). These in situ estimates agree with the present model outcomes, ensuring that the intrinsic VLFs in the transient rip currents are substantially excited by bathymetric variability.

5. Decay of Unforced Eddies

5.1. Spin-Down Experiment

The intrinsically unstable rip currents comprise significant three-dimensionality as shown in Figures 3 and 4, whereas the barotropic analyses in the preceding sections do not fully capture it. To see the 3-D effects in the rip currents more closely, we introduce a pseudo 2D (P2D) model based on the fully 3-D model by constraining the vertical eddy viscosity K_v not to be below 0.1 m^2/s everywhere, while it may lead to inconsistent bottom stress through altered velocity vertical shear. Nevertheless, the P2D model enables us to practically eliminate the depth-dependency from the 3-D case, which mimics the 2-D barotropic model quite well. Because the wave forcing keeps generating eddies through the vorticity source curl **B** (section 4.2) and hinders most of the three-dimensionality, we focus on initial development and subsequent decay of rip currents and associated coherent eddies. Hence, we carry out a spin-down experiment by imposing the wave forcing until $t = 5$ min to initiate offshore-directed rip jets and associated vortices, after which the forcing is abruptly turned off to let eddies decay spontaneously. This spin-down test is somewhat similar to the 2-D numerical experiment for the self-excitation of the offshore shedding of a forced single vortex dipole in *Geiman and Kirby* [2013], although we aim to retain three-dimensionality, the wave-induced rip currents, and the realistic bathymetric information.

Figure 14 is sequential snapshots of the barotropic vorticity q in the 3-D and 2-D (i.e., P2D) cases with and without the wave forcing for $t \geq 5$ min. At $t = 5$ min, all the 4 cases show almost identical vorticity fields with a rip current and an associated seaward elongated vortex pair around $y = 420$ m. In the forced cases the vortices are readily unstable, forming meanders and roll-up while the rip current develops. Apparently

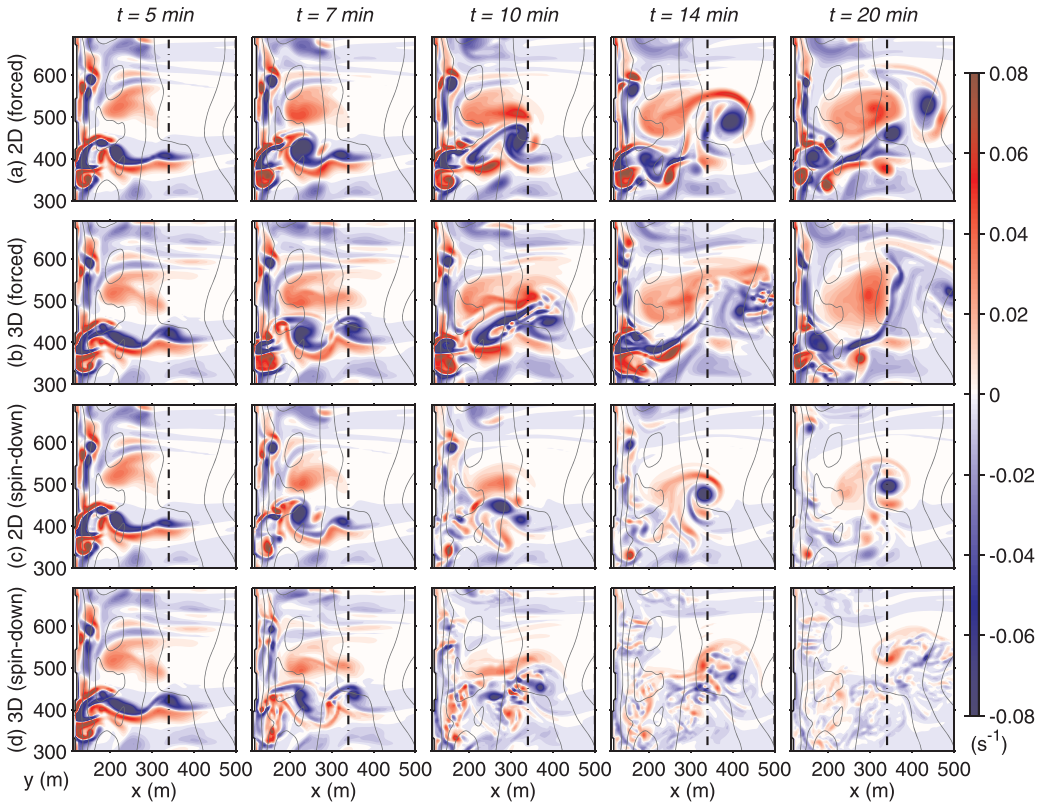

Figure 14. Sequential snapshots of barotropic relative vorticity $q=\nabla_H\times\ \mathbf{u}_{bt}$ during the initial development of rip currents at $t = 5$, 7, 10, 14 and 20 min for (a) the pseudo 2D (P2D) forced, (b) 3-D forced, (c) pseudo 2D spin-down, and (d) 3-D spin-down cases. The vertical dashed lines denote the approximate offshore extents of the inner surf zone ($x < 340$ m). The wave forcing vanishes after $t \geq 5$ min for the two spin-down cases to let eddies decay spontaneously, whereas the steady forcing is imposed all the time for the two forced cases. The P2D model is run with constrained eddy viscosity in the fully 3-D model to suppress depth-dependency, mimicking the 2-D barotropic model. Notice that the forced 3-D vortices are significantly elongated in the longitudinal direction, while the unforced 3-D vortices are promptly collapsed into smaller eddies, as compared to more coherent, long-lived 2-D vortices.

the forced 2-D eddies are more coherent than the forced 3-D eddies, consistent with Figure 5. The 3-D eddies are then stretched northeastward remarkably at $t \geq 14$ min to evolve into a filament rather than circular vortices. In the unforced cases the 3-D eddies evidently break down into small eddies and decay much more quickly than the 2-D eddies for $t \geq 5$ min. The unforced 2-D eddies retain coherent structures even at $t = 20$ min, indicating longer lifetimes and larger wavelengths.

5.2. Kinetic Energy Wavenumber Spectra

Spatiotemporal evolution of coherent eddies in transient rip currents are diagnosed with the alongshore-wavenumber barotropic kinetic energy (KE_{bt}) spectra, S_{bt}, at $x = 140$, 240, and 360 m, and at $t = 5$, 20, and 50 min (Figure 15). We focus on the unforced spin-down cases to observe the fate of eddies to avoid the complexities associated with the wave forcing that keeps recharging kinetic energy in the lower wavenumbers in the forced cases. At $t = 5$ min, the spectral shapes of the P2D and 3-D models are almost identical as intended. The peak wavelength is evident, ranging between 90 and 160 m. In the P2D model, as the KE_{bt} gradually decreases with time, the peak wavelength increases due to the KE_{bt} transferred to the lower wavenumbers. In contrast, the 3-D model more rapidly loses the KE_{bt} particularly at the lower wavenumbers. The KE_{bt} is transferred to the higher wavenumbers as most notably seen in (c), making mean spectral slopes gentler than the P2D model. Hence, the 2-D eddies are dominated by the inverse kinetic energy cascade, resulting from growth and merging of initially smaller nearshore vortices that travel offshore and evolve into coherent rolled-up circular eddies. In contrast, the 3-D eddies readily break down into smaller eddies with time and further collapse to promote the transfer of the KE_{bt} to the higher wavenumbers.

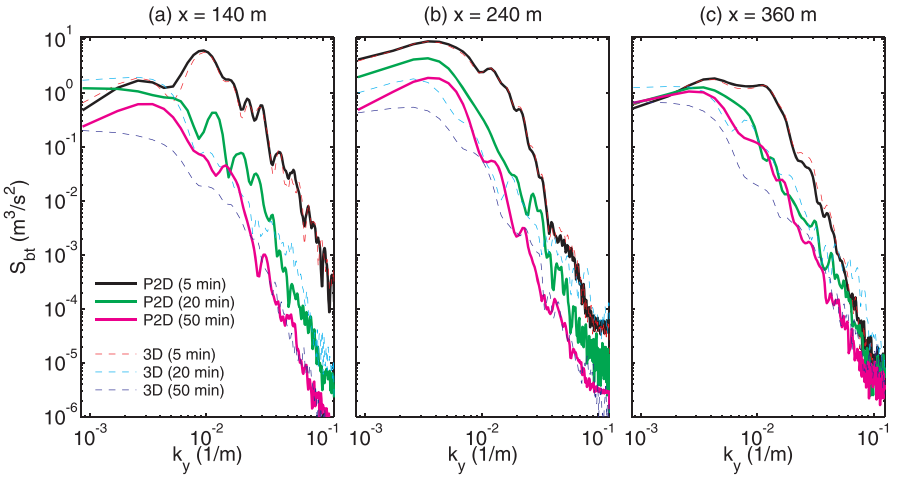

Figure 15. Alongshore-wavenumber barotropic kinetic energy spectra S_{bt} for the P2D (thick solid curves) and 3-D (thin dotted curves) spin-down cases at $t = 5$, 20, and 50 min denoted by the legend in Figure 15a. The selected cross-shore locations are at (a) $x = 140$ m in the *feeder* region, where the shore-face breaking occurs (Figure 2b), (b) $x = 240$ m in the inner surf zone (Figure 2c), and (c) $x = 360$ m in the offshore *rip-head* region. The abscissae are the reciprocal wavelength in m^{-1}. Initially, the peak wavelength is evident, ranging between 90 and 160 m. In the P2D model, the peak wavelength increases due to the kinetic energy transfer to the lower wavenumbers. In contrast, the 3-D model rapidly loses the kinetic energy in the lower wavenumbers that is transferred to the higher wavenumbers as most notably seen in (c), resulting in gentler spectral slopes than the P2D model.

5.3. 3-D Vorticity Analysis

To further examine three-dimensionality of the rip eddies during the spin-down, we conduct a 3-D vorticity analysis, in which the wave forcing terms (section 4.2) vanish to simplify the vorticity equation. For the incompressive ($\rho = \rho_0$: constant), nonrotating ($f_c = 0$), unforced 3-D fluid, the vorticity equation for the vertical relative vorticity ω_z may be reduced to:

$$\underbrace{\partial_t \omega_z}_{\text{tendency}} \underbrace{+(\mathbf{u}\cdot\nabla)\omega_z}_{\text{advection}} = \underbrace{\omega_x \partial_x w + \omega_y \partial_y w}_{\text{vortex tilting}} \underbrace{-\omega_z(\partial_x u + \partial_y v)}_{\text{vortex stretching}} \underbrace{+\partial_z(K_v \partial_z \omega_z)}_{\text{diffusion}} \tag{8}$$

where $\boldsymbol{\omega} = \nabla \times \mathbf{u} = (\omega_x, \omega_y, \omega_z)$: the vorticity. The first RHS terms represent vortex tilting, which translates ω_x and ω_y into ω_z due to inclination of the vertically oriented vortices. The second RHS term is the vortex stretching term that acts to alter ω_z due to the vertical compaction and expansion of the vortices associated with divergence of the lateral flow in order to keep the circulation constant. The third RHS, the vertical diffusion term, is also included to investigaete because we intentionally alter the vertical eddy viscosity K_v for the P2D model.

Figure 16 shows a snapshot of $\boldsymbol{\omega}$ and the tilting and stretching terms at $z = -0.8$ m at $t = 10$ min (i.e., 5 min after turning off the wave forcing) when eddies start to diminish. The P2D model successfully reduces the depth-dependency during the spin down, as ω_x and ω_y practically vanish (Figure 16). The horizontal vorticity is very large in the 3-D model and a factor of 4–5 larger than the vertical vorticity, due primarily to the vertical shear of the horizontal velocities. It is obvious that the vortex titling and stretching terms in the 3-D case dominate over the 2-D case, promoting the forward KE cascade (Figure 15), where the initially coherent eddies collapse into smaller eddies more promptly than the 2-D case. The depth-dependent rip currents are accompanied by strong ω_x and ω_y as counter-rotating streamwise vortex pairs (Figures 4 and 16b) that easily yield the tilting effects to modify ω_z. The stretching term is also significant, while it is more intensified in the 3-D case than the 2-D case, because the offshore eddy migration preconditions vortex stretching due to the increased depth.

The vertical cross-sectional plots of all the three RHS terms and the advection term in equation (8) at $t = 10$ min are shown in Figure 17 along the transect at $y = 454$ m (Figure 16). The P2D model generates the depth-invariant ω_z, which is primarily maintained by the balance between the advection and the tendency (not shown). The tilting term vanishes, while the stretching term moderately contributes, for example, to enhance the negative ω_z centered at $x = 290$ m traveling offshore. Evidently, the 3-D model yields considerable depth-dependency in ω_z and all the terms. Although the primary balance occurs between the advection and tendency terms, the depth-variant tilting and stretching terms concurrently contribute to the 3-D vorticity balance. For instance, the negative ω_z on the seaward side of the vortex pair at $x = 200$ m is

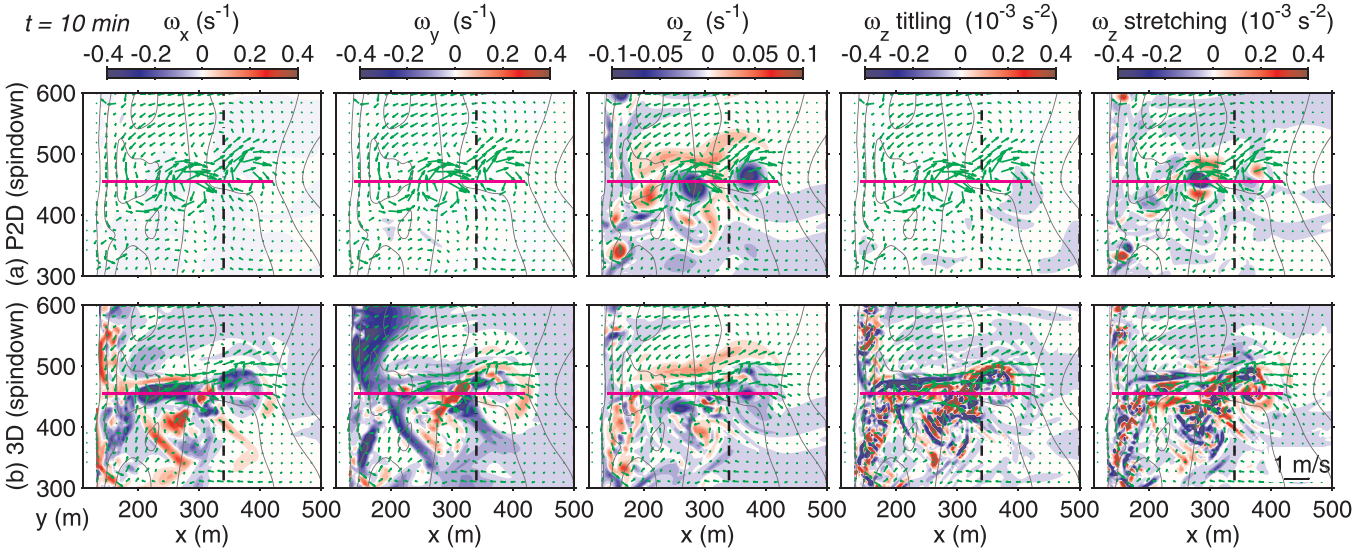

Figure 16. Snapshots of the subsurface vorticity ω_x, ω_y, ω_z, the vortex tilting and stretching terms in the ω_z conservation equation (equation (8)) at $t = 10$ min (*i.e.*, 5 min after vanishing the wave forcing) at $z = -0.8$ m for (a) the pseudo 2D and (b) 3-D spin-down cases. Horizontal velocity vectors $\mathbf{u}_H$ at $z = -0.8$ m subsampled every 4-grid points are overlaid (green). The vertical dashed lines denote the approximate offshore extents of the inner surf zone ($x < 340$ m). The horizontal magenta lines define the cross-section at $y = 454$ m used in Figure 17. The constrained vertical eddy viscosity in the pseudo 2D model successfully diminishes ω_x and ω_y components of the 3D vortices arising from the depth-dependency, leading to negligibly small ω_z tilting effects. Notice that the 3-D rip current is associated with counter-rotating longitudinal vorticity composed of ω_x and ω_y.

enhanced by the tilting and stretching terms near the surface, whereas reduced by the positive stretching near the bed, resulting in the seaward inclination of the vortex tube as shown by the advection. As a consequence, ω_z is converted into ω_x and ω_y to provoke the vertical circulations, and ω_z is diminished accordingly. In other words, the vortex tilting helps to make the 2-D eddies ($\omega_z \gg \omega_x, \omega_y$) transform the 3-D eddies ($\omega_z \approx \omega_x, \omega_y$) to readily collapse into smaller eddies due to the forward energy cascade. In contrast, the diffusion term plays a minor role in the vorticity budget, even though the present model does not account for spatiotemporal evolution of K_v due to such as the offshore transport of EKE [e.g., *Kumar and Feddersen*, 2017a,2017b]. The nonwave, shear-induced K_v profiles evaluated by the standard KPP model provide $1\text{–}6 \times 10^{-3}$ m^2/s (cf. Figure 3a in UMS10) with the incremental near-surface intensification of an additional $\sim 7 \times 10^{-3}$ m^2/s due to the wave breaking (cf. Figure 3c in UMS10). The parabolic vertical shape of the

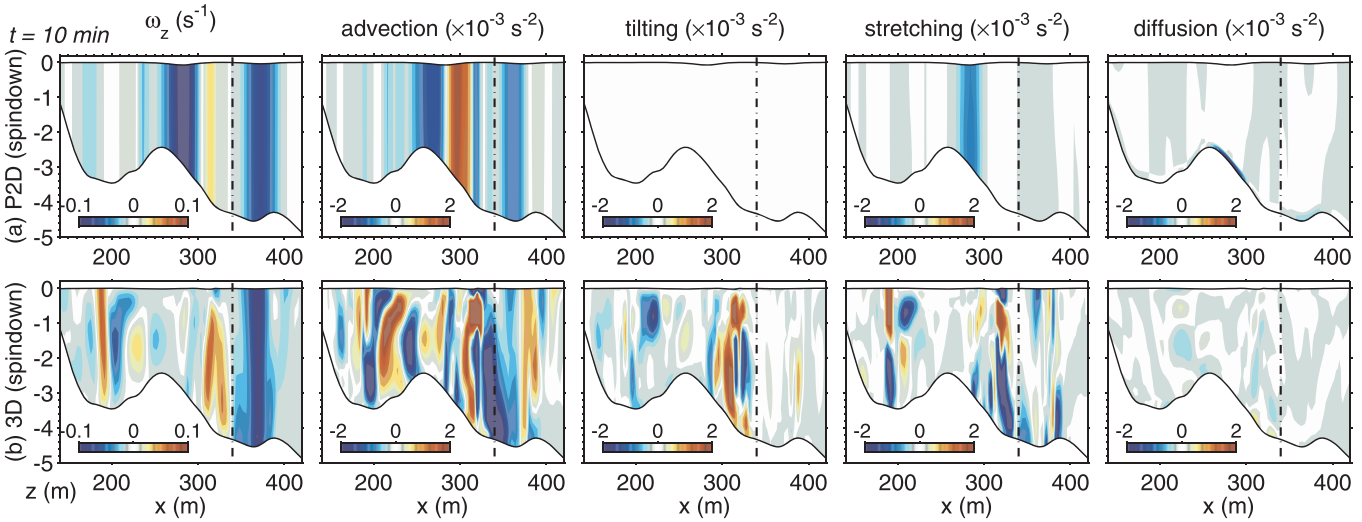

Figure 17. Snapshots of ω_z and the terms in the unforced 3-D vorticity equation (8) at $t = 10$ min along the cross section at $y = 454$ m defined in Figure 16 for (a) the pseudo 2D and (b) 3-D spin-down cases. The P2D model yields the depth-invariant ω_z and the negligibly small tilting effects. The 3-D vorticity is generally depth-dependent, and so are the associated vorticity terms. The diffusion terms for both models are relatively minor and do not play an essential role.

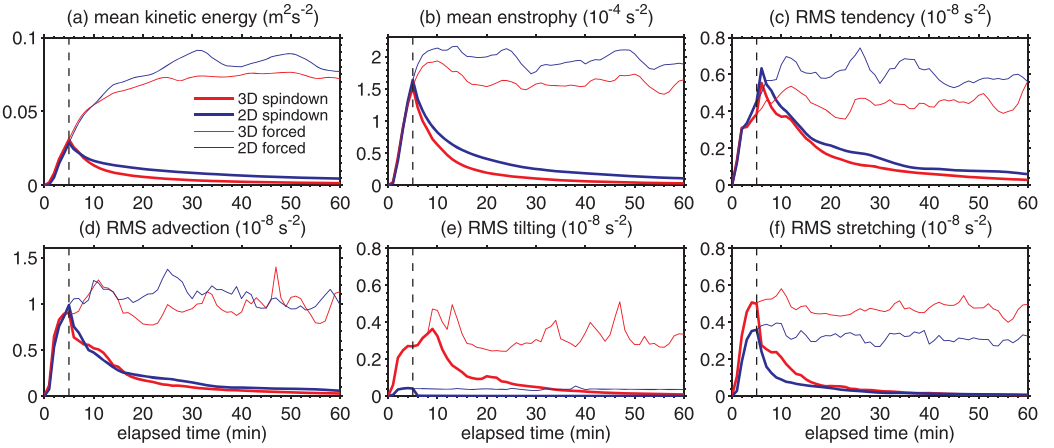

Figure 18. Time series plots of the volume-averaged (a) kinetic energy and (b) enstrophy of ω_z, and the lateral standard deviations of the depth-averaged terms in the ω_z equation (8): (c) the tendency, (d) the advection, (e) the vortex tilting, and (f) the vortex stretching, for the 3-D (red) and pseudo 2D (blue) cases. Bold and thin lines represent the spin-down and forced cases. The vertical dotted lines are the timing when the forcing is shut off at $t = 5$ min. The volume averages and lateral standard deviations are taken for $x \leq 600$ m. The 3-D cases indicate pronounced effects from the vortex titling and stretching on ω_z. The former is more substantially reduced than the latter in the P2D cases.

nonwave K_v is retained with a gradual decrease of its magnitude even after the forcing is shut off. The imposed lower limit of 0.1 m^2/s for the K_v in the P2D model acts to vertically redistribute the vorticity and consequently, reduces the diffusion term.

To extend the above arguments to the temporal evolution of the vorticity balance, the 3-D vorticity terms for both the forced and the unforced spin-down cases are depicted in Figure 18, along with the volume-averages of the barotropic kinetic energy KE_{bt} and enstrophy of ω_z. Note that the vorticity terms (Figures 18c–18f) are represented as the lateral standard deviations of the depth-averages of each term, as proxies for the volume averaged magnitudes. The 2-D eddies are more energetic and long-lived as depicted in the KE_{bt}, the enstrophy, and the tendency term regardless of wave forcing. Although the differences of the advection terms are subtle for each case, the tilting and stretching terms are concurrently intensified in the 3-D cases and moderately contribute to the vorticity tendency. In particular, the tilting term is apparent in the 3-D cases as intended, leading to the faster decay of the 3-D eddies. The tilting is initially magnified by $t = 10$ min, and subsequently, gradually decreases for about 20 min for the 3-D spin-down case, which is sufficiently long and is comparable to the mean VLF period of about 18 min (section 4.3) to interact with the VLFs. For the forced cases, each of the advection and stretching terms fluctuates similarly in the 2-D and 3-D models. The stretching term is amplified ~25% in the 3-D forced case relative to the 2-D, due to the vortex expansion and compaction, which eventually is compensated for by the tendency term.

6. Conclusions

The ROMS-WEC model [*Uchiyama et al.*, 2010] based on an Eulerian wave-averaged vortex-force asymptotic theory of MRL04 is applied to analyze the transient wave-driven 3-D rip currents that spontaneously occur on a surveyed sandy-beach bathymetry at Duck, NC, under spatiotemporally uniform offshore incident waves. Substantial depth-dependency is demonstrated in the vertical profiles of the rip currents that concentrate at 1–3 m below the surface due to the surf-zone recirculation associated with the surface-confined breaker acceleration and the near-bed undertow. The 3-D rip currents are composed of pairs of counter-rotating longitudinal overturning roll cells that promote surface convergence along the rip center. A vorticity budget analysis exhibits that the vortex force torque plays the most dominant role other than the breaker acceleration torque that is the primary source of vorticity and, thus, the eddy kinetic energy (EKE) production responsible for the rip eddy shedding. Overall, the vortex force torque preconditions vorticity reduction from the rip eddies, while it conversely recharges vorticity to the rip eddies in the shoreward of the wave breaking points where reformation of the broken waves occurs.

These rip currents are intrinsically unstable either in the 3-D or 2-D models. The fluctuations of the transient rip currents are significant, contributing about 70% of kinetic energy (KE) as EKE. The contribution to the generation of the EKE and the Reynolds stress from the depth-variant velocity is evaluated for 5–6%. The dominant fluctuation period is estimated at about 18 min, but the energy is extensively distributed in broadband in the frequency space. If we define our VLF (very low frequency) band for the periods between 5 and 100 min, the EKE contained in the VLF explains about 70% of the total EKE. The modeled *intrinsic* EKE in the VLF band is quantitatively comparable to that of the rotational VLFs observed on the same beach [e.g., *MacMahan et al*., 2010b; *de Schipper et al*., 2012], clarifying that bathymetric variability is the main source of the *intrinsic* VLFs. In addition, the VFLs due to group waves [e.g., *Long and Özkan-Haller*, 2009] and individual breaking waves [e.g., *Spydell and Feddersen*, 2009], both of which are neglected in the present model, are anticipated to further excite the *forced* VLFs. The mean *intrinsic* VLF period is consistent with those for the sinuous mode Bickely jet and the Karman vortex streets in wakes and shear turbulence, which suggests shear instability primarily controls the intrinsic VLF variability. Supplemental numerical experiments illustrate that the feedback mechanism of the current effect on waves (CEW) [cf. *Uchiyama et al*., 2009] alters not only the mean rip current structure but also the associated turbulence field. The former has been well known as the attenuation effects of CEW on rip currents [cf. *Yu and Slinn*, 2003; *Weir et al*., 2011]. The latter modifies the cross-shore EKE profile prominently with considerable accentuation of the eddying motions near the shore (*feeder* region) and in the inner surf zone centered at the inner bar (*neck* region), owing to shoreward contraction effects of CEW that hinder the offshore EKE transport. Moreover, alongshore bathymetric variability is explicitly demonstrated as an important factor that intensifies KE and EKE with increased alongshore undulations.

The 2-D model generates more coherent, organized, long-lived, and circular eddies. The 3-D eddies are rather stretched laterally, resulting in elongated filaments and streaks. The underlying mechanism is examined through a spin-down experiment, where a pseudo 2D model is configured based on the 3-D model with an incremental background vertical eddy viscosity for quantitative comparisons with the fully 3-D model. Because the horizontal vorticity components are inherent in the 3-D transient rip currents, the vortex tilting effect enters vorticity budgets and plays an inevitable role, together with the vortex stretching effects, in collapsing 3-D eddies to enhance forward kinetic energy cascade. As a consequence, the 3-D eddies are short-lived and decay more quickly than the 2-D eddies.

Appendix A: The ROMS-WEC Model

The prognostic variables in the ROMS-WEC are the wave-averaged 3-D Eulerian velocity $\mathbf{u} = (\mathbf{u}_H, w) = (u, v, w)$ and the wave-averaged sea surface elevation ζ^c. The former is related to the 3-D Lagrangian velocity $\mathbf{u}^l = (\mathbf{u}_H{}^l, w^l) = (u^l, v^l, w^l)$ and the nondivergent 3-D Stokes drift velocity $\mathbf{u}^{St} = (\mathbf{u}_H{}^{St}, w^{St}) = (u^{St}, v^{St}, w^{St})$ by $\mathbf{u}^l = \mathbf{u} + \mathbf{u}^{St}$. All the governing equations are expressed in horizontal curvilinear coordinate and vertically stretched surface- and terrain-following s coordinate [*Shchepetkin and McWilliams*, 2005], which is defined by ζ^c and the depth h with the transformed grid-cell thickness H_z^c. The wave-averaged continuity equation is expressed in the horizontal Cartesian and the vertical s coordinates for the brevity:

$$\partial_t H_z^c + \nabla_H \cdot \left(H_z^c \mathbf{u}_H^l\right) + \partial_s\left(\omega_s^l\right) = 0, \tag{A1}$$

where ω_s^l: the vertical motion passed s surface related to w^l through equation (32) of UMS10; and $\nabla_H = \left(\partial_x,\ \partial_y\right)$: the horizontal gradient operator. Similarly, the horizontal momentum equation is

$$\begin{aligned} &\partial_t\left(H_z^c \mathbf{u}_H\right) + \partial_x\left(H_z^c u^l \mathbf{u}_H\right) + \partial_y\left(H_z^c v^l \mathbf{u}_H\right) + \partial_s\left(\omega_s^l \mathbf{u}_H\right) \\ &= H_z^c\left[-f_c \hat{\mathbf{z}} \times \mathbf{u}_H^l - \nabla_H \phi^c + \tilde{\mathbf{u}}_H^{St} \cdot \nabla_H \tilde{\mathbf{u}}_H + \mathbf{F} + \mathbf{F}^w\right], \end{aligned} \tag{A2}$$

where f_c: the Coriolis parameter; $\hat{\mathbf{z}}$: the vertical unit vector pointing upward; and $\mathbf{F}$: nonwave nonconservative body forces including parameterized momentum mixing terms. The tilde convention identifies conjoined horizontal vectors in a dot product. $\mathbf{F}^w$ is the wave-induced nonconservative body forces from depth-induced breaking, surface rollers, wave-induced boundary streaming, and the incremental breaking-enhanced vertical mixing in the KPP model [*Large et al*., 1994; *Durski et al*., 2004]. In the present study, however, the first three contributions are alternatively imposed as the equivalent surface and bottom stress boundary conditions of $\mathbf{u}_H$ (Appendix C) instead of as the body forces for satisfactory reproducibility with in situ data even though vertical grid resolution is not fine enough with fewer tuning parameters (n.b., UMS10, sections 3.3, 4.4, and 4.6). The vertical momentum equation appears in the wave-averaged hydrostatic balance, leading to the wave-enhanced geopotential function ϕ^c:

$$\phi^c = g\left(\zeta^c - \hat{\zeta}\right) - (\mathcal{P} - \mathcal{K})|_{\zeta^c} + \int_s^0 \left[\frac{\rho g}{\rho_0} - K\right] H_z^c ds, \tag{A3}$$

where g: the gravity; ρ: the density of the sea water; ρ_0: the reference density (1027.5 kgm^{-3}); $\hat{\zeta}$: the quasi-static surface elevation known as wave set-down; $\mathcal{P}$: the pressure correction from the interaction between vertical current shear and depth-dependent Stokes drift; $\mathcal{K}$: the Bernoulli head after subtracting $\hat{\zeta}$; and K: the vertical vortex force (n.b., MRL04, section 9.6; UMS10, sections 2.1 and 2.2).

Appendix B: The Barotropic ROMS-WEC Model

The barotropic version of ROMS-WEC model has previously been developed and used in UMR09 for 2-D shear waves with a vortex force formalism and its prototype was provided in *Uchiyama and McWilliams* [2008] in the context of excitation and propagation of the oceanic infragravity long waves. The governing continuity and horizontal momentum equations of the wave-averaged barotropic model are expressed in the horizontal Cartesian coordinate as:

$$\partial_t \ \zeta^c + \nabla_H \cdot \left(D\mathbf{u}_{bt}^l\right) = 0, \tag{A4}$$

$$\begin{aligned} &\partial_t \mathbf{u}_{bt} + (\mathbf{u}_{bt} \cdot \nabla_H)\mathbf{u}_{bt} \\ &= -f_c \hat{\mathbf{z}} \times \mathbf{u}_{bt}^l - g\nabla_H\left(\zeta^c - \hat{\zeta}\right) - \hat{\mathbf{z}} \times \mathbf{u}_{bt}^{St}(\nabla_H \times \mathbf{u}_{bt}) + \frac{\boldsymbol{\tau}_{sur}}{\rho_0 D} - \frac{\boldsymbol{\tau}_{bot}}{\rho_0 D}, \end{aligned} \tag{A5}$$

where $\mathbf{u}_{bt} = (u_{bt}, \ v_{bt})$: depth-averaged, barotropic 2-D Eulerian current velocity; $\mathbf{u}_{bt}^{St} = \left(u_{bt}^{St}, v_{bt}^{St}\right)$: the depth-averaged Stokes transport; $\mathbf{u}_{bt}^l = \left(u_{bt}^l, v_{bt}^l\right) = \mathbf{u}_{bt} + \mathbf{u}_{bt}^{St}$: barotropic 2-D Lagrangian current velocity; $D = h + \zeta^c$: the wave-averaged height of the water column; $\boldsymbol{\tau}_{sur}$: the surface stress; and $\boldsymbol{\tau}_{bot}$: the bed stress. The prognostic variables of the barotropic 2-D ROMS-WEC are $\mathbf{u}_{bt}$ and ζ^c. In the present study we discretize the barotropic advection term with a third-order upwind scheme equivalent to that used in the ROMS. Hence, the momentum equation slightly differs from that in UMR09 in which the centered advection scheme requires an additional lateral harmonic mixing term to suppress dispersive artifacts (n.b., UMR09, equation (3)).

Appendix C: Boundary Conditions

Following UMS10 (section 3.3), the bed stress $\boldsymbol{\tau}_{bot}$ used in the bottom boundary condition for $\mathbf{u}_H$ is given as the sum of the bottom streaming stress $\boldsymbol{\tau}_{bot}^{wd}$ and the combined wave-current bottom drag $\boldsymbol{\tau}_{bot}^{cd}$. In the present study we employ a formula for $\boldsymbol{\tau}_{bot}^{cd}$, proposed originally by *Feddersen et al.* [2000], who optimized it for the data set obtained during the *SandyDuck* experiment in Duck, NC.

$$\boldsymbol{\tau}_{bot} = \boldsymbol{\tau}_{bot}^{wd} + \boldsymbol{\tau}_{bot}^{cd} = \frac{\epsilon^{wd}}{\sigma}\mathbf{k} + 0.015 \ \rho_0 \left(\frac{k_a}{D}\right)^{1/3} \left[1.35 + \left(\frac{|\mathbf{u}_{bt}|}{|\mathbf{u}_{rms}^w|}\right)^2\right]^{1/2} |\mathbf{u}_{rms}^w| \mathbf{u}_{bt}, \tag{A6}$$

where ϵ^{wd}: the wave bottom drag dissipation [*Thornton and Guza*, 1983; UMS10, section 3.2]; σ: the intrinsic wave frequency; $\mathbf{k} = (k_x, \ k_y)$: wavenumber vector of the primary wave whose magnitude is k; k_a: the apparent roughness (=0.0125 m) [*Ruessink et al.*, 2001]; $\mathbf{u}_{rms}^w = \mathbf{u}_{orb}^w/\sqrt{2}$: the RMS wave orbital velocity at the bed; $\mathbf{u}_{orb}^w = \sigma H_{rms}/\sinh kD \cdot \mathbf{k}/k$: the wave orbital velocity at the bed; and H_{rms}: the RMS wave height. For better reproducibility with the observation, we alternatively employ the bottom-most horizontal velocity instead of $\mathbf{u}_{bt}$ in the 3-D ROMS-WEC model to best fit the field data (not shown). Notice that *Feddersen et al.* [2000] only parameterized the quadratic velocity moment for the alongshore momentum balance, while the model applies to both horizontal balances as pointed out in *Long and Özkan-Haller* [2009].

The surface boundary condition for $\mathbf{u}_H$ is similarly given by the surface stress $\boldsymbol{\tau}_{sur}$ as the sum of $\boldsymbol{\tau}_{sur}^{wind}$: surface wind stress, and $\boldsymbol{\tau}_{sur}^b$: the stress-form of the nonconservative WEC body forces from depth-induced wave breaking ϵ^b and the surface roller ϵ^r (see UMS10, section 3.2).

$$\boldsymbol{\tau}_{sur} = \boldsymbol{\tau}_{sur}^{wind} + \boldsymbol{\tau}_{sur}^b = \boldsymbol{\tau}_{sur}^{wind} + \frac{(1-\alpha_r)\epsilon^b + \epsilon^r}{\sigma}\mathbf{k}, \tag{A7}$$

where α_r: the fraction of ϵ^b converted into surface rollers.

All the numerical simulations are carried out in rectangle domains with the shore to the west and the offshore open boundary to the east in the x direction. The alongshore-periodic condition is imposed in the y

direction. At the shoreline represented by the land-mask function, there is a zero cross-shore mass flux: $u+u^{St}=0$ and $u_{bt}+u_{bt}^{St}=0$ with $u^{St}\approx 0$ and $u_{bt}^{St}\approx 0$ as for strong dissipation by wave breaking; no tangential flow: $v=0$ and $v_{bt}=0$; and the Neumann condition: $\partial_x\zeta=0$. Chapman-type radiation boundary conditions are adapted for ζ^c, u and u_{bt} at the offshore open boundary with weak nudging toward $\hat{\zeta}+\zeta$, $-u^{St}$ and $-u_{bt}^{St}$, where ζ is a nonwave free surface elevation such as due to tides, which is assumed time-invariant in the present study (Table 1). The Neumann condition is used for all the other variables at the offshore boundary. The minimum water depth is set to 0.1 m, and movement of the shoreline, due to wetting and drying, is not considered.

Appendix D: The WKB Spectrum Peak Wave Refraction Model

For a narrow-banded, spectrum peak wave field, we exploit a set of ray equations based on the WKB approximation [e.g., *Mei*, 1992] for refractive wave transformation by the conservation equations of wave action density $\mathcal{A}=\rho_0 g H_{rms}^2/8\sigma$ and the wavenumber $\mathbf{k}$ as

$$\partial_t\mathcal{A}+\nabla_H\left[\left(\mathbf{c}_g+\mathbf{u}_{bt}\right)\mathcal{A}\right]=-\frac{1}{\sigma}\left(\epsilon^b+\epsilon^{wd}\right), \tag{A8}$$

$$\partial_t\mathbf{k}+\left(\mathbf{c}_g+\mathbf{u}_{bt}\right)\cdot\nabla_H\mathbf{k}=-\tilde{\mathbf{k}}\cdot\nabla_H\tilde{\mathbf{u}}_{bt}-\frac{k\sigma}{\sinh\,2kD}\nabla_H D, \tag{A9}$$

where $\mathbf{c}_g$: (non-Doppler shifted) group velocity, and the tilde convention is the same as that in equation (A2) in Appendix A. With the linear dispersion relation, the Doppler-shifted wave frequency σ_{ds} is represented as

$$\sigma_{ds}=\mathbf{u}_{bt}\cdot\mathbf{k}+\sigma=\mathbf{u}_{bt}\cdot\mathbf{k}+\sqrt{gk\tanh kD}. \tag{A10}$$

To better estimate the surf zone wave field, the surface roller model [*Svendsen*, 1984; UMS10, section 3.2] can be exploited.

$$\partial_t\mathcal{A}^r+\nabla_H[(\mathbf{c}+\mathbf{u}_{bt})\mathcal{A}^r]=-\frac{1}{\sigma}\left(\epsilon^r-\alpha_r\epsilon^b\right), \tag{A11}$$

where $\mathcal{A}^r$: roller action density; $\mathbf{c}=\sigma k^{-2}\mathbf{k}$: the phase velocity of the primary wave (notice not $\mathbf{c}_g$ [*Svendsen*, 1984], but $\mathbf{c}\approx\mathbf{c}_g$ anyway for $kD\rightarrow 0$); and $\epsilon^r=gk\mathcal{A}^r\sin\beta$: a parameterized roller dissipation rate. According to *Nairn et al*. [1991] and *Apotsos et al*. [2007], we rely on $\alpha_r=1$ and $\sin\beta=0.1$. The depth-dependent Stokes drift and its depth-average are then expressed as

$$\mathbf{u}_H{}^{St}(z)=\frac{\sigma^2\cosh 2k(z+h)}{\rho_0 g\sinh^2 kD}(\mathcal{A}+\mathcal{A}^r)\mathbf{k};\quad \mathbf{u}_{bt}^{St}=\frac{(\mathcal{A}+\mathcal{A}^r)}{\rho_0 D}\mathbf{k}\ . \tag{A12}$$

The breaker dissipation ϵ^b is determined by a quasi-empirical parameterization for Rayleigh distributed narrow banded waves described in *Church and Thornton* [1993]:

$$\epsilon^b=\rho_0 g\frac{3\sqrt{\pi}}{16}\frac{B_b^3\sigma}{2\pi D}H_{rms}^3\left[1+\tanh\left\{8\left(\frac{H_{rms}}{\gamma_b D}-1\right)\right\}\right]\cdot\left[1-\left\{1+\left(\frac{H_{rms}}{\gamma_b D}\right)^2\right\}^{-5/2}\right], \tag{A13}$$

where B_b and γ_b are empirical constants depending on a beach profile and the type of breaker.

The wave model is solved at every baroclinic time step for the 3-D cases, while it is solved at every barotropic time step for the 2-D cases as a subroutine in the ROMS-WEC with the same thread structure and, thus, is identically parallelized. The computational cost of the wave model is negligibly cheaper than the 3-D ROMS-WEC, whereas it typically takes about 80% as much as the barotropic current model. We choose the alongshore-periodic condition and the shoreline Neumann condition for all the wave variables. The offshore clamped conditions for $\mathcal{A}$ and $\mathbf{k}$ with prescribed incident wave parameters of H_{rms}, σ, and the wave direction θ_p are used. The feedback mechanisms of CEW participate in the wave model through the Doppler shift due to $\mathbf{u}_{bt}$ and wave-averaged surface elevation ζ^c, hence in D. Note that the present wave model solutions do not generate caustics or other ray singularities with our particular choices of incident waves and bathymetries.

Acknowledgments
This research is supported by the JSPS Grants-in-Aid for Scientific Research 15KK0207 and 15H04049 at Kobe University, NSF OCE-1355970 and ONR N00014–15-1–2645 at UCLA, and NSF XSEDE computing resources. M. Kawakami of Kobe University carried out the preliminary simulations in Secs 4.3 and 4.4. F. Feddersen of Scripps Institution of Oceanography provided knowledgeable comments on the manuscripts that improve the clarity of the study. We are grateful for Office of Naval Research, U.S. Army Corps of Engineers, S. Elgar, R. T. Guza, T. H. C. Herbers, P. A. Howd, K. K. Hathaway, W. A. Birkemeier, C. E. Long and other scientists and staff involved in the *SandyDuck* experiment and the bathymetry surveys around the Field Research Facility for making their data set available. The surveyed data used in the present study are archived at http://navigation.usace.army.mil/CHL_Viewer/FRF/. The source code for the ROMS-WEC model is available from the authors upon request (uchiyama@harbor.kobe-u.ac.jp).

References

Aagaard, T., B. Greenwood, and J. Nielsen (1997), Mean currents and sediment transport in a rip channel, *Mar. Geol.*, *140*, 25–45.
Allen, J. S., P. A. Newberger, and R. A. Holman (1996), Nonlinear shear instabilities of alongshore currents on plane beaches, *J. Fluid Mech.*, *310*, 181 – 213.
Apotsos, A., B. Raubenheimer, S. Elgar, R. T. Guza, and J. A. Smith (2007), Effects of wave rollers and bottom stress on wave setup, *J. Geophys. Res.*, *112*, C02003, doi:10.1029/2006JC003549.
Ardhuin, F., N. Rascle, and K. A. Belibassakis (2008), Explicit wave-averaged primitive equations using a generalized Lagrangian mean, *Ocean Modell.*, *20*, 35–60.
Bearman, P. W. (1967), On vortex street wakes, *J. Fluid Mech.*, *28*, 625–641.
Bonneton, P., N. Bruneau, B. Castelle, and F. Marche (2010), Large scale vorticity generation due to dissipating waves in the surf zone, *Discrete Contin. Dyn. Syst., Ser. B*, *13*(4), 729–738, doi:10.3934/dcdsb.2010.13.729.
Bowen, A. J. (1969), Rip currents, 1, Theoretical investigations, *J. Geophys. Res.*, *74*, 5467–5478.
Bowen, A. J., and R. A. Holman (1989), Shear instabilities of the mean longshore current: 1. Theory, *J. Geophys. Res.*, *94*, 18,023–18,030.
Brander, R. W., and A. D. Short (2001), Flow kinematics of low-energy rip current systems, *J. Coastal Res.*, *17*(2), 468–481.
Bruneau, N., P. Bonneton, B. Castelle, and R. Pedreros (2011), Modeling rip current circulations and vorticity in a high-energy mesotidal-macrotidal environment, *J. Geophys. Res.*, *116*, C07026, doi:10.1029/2010JC006693.
Church, J.C. and E.B. Thornton (1993), Effects of breaking wave induced turbulence within a longshore current model, *Coastal Eng.*, *20*, 1–28.
de Schipper, M. A., A. Reniers, J. MacMahan, and R. Ranasinghe (2012), Vortical VLF motions under shore-normal incident waves, in Proceedings of 33rd International Conference on Coastal Engineering, edited by P. Lynett and J. M. Smith, International Conference on Coastal Engineering (ICCE), 13 pp., Santander, Spain, doi:10.9753/icce.v33.waves.58.
Dodd, N., J. Oltman-Shay, and E. B. Thornton (1992), Shear instabilities in the longshore current: A comparison of observation and theory, *J. Phys. Oceanogr.*, *22*, 62–82.
Dodd, N., J. Oltman-Shay, and E. B. Thornton (1994), On the destabilization of a longshore current on a plane beach: Bottom shear stress, critical condition and onset of instabilities, *J. Geophys. Res.*, *99*, 811–824.
Dodd, N., V. Iranzo, and A. Reniers (2000), Shear instabilities of wave-driven alongshore currents. *Rev. Geophys.*, *38*, 437–464.
Durski, S. M., S. M. Glenn, and D. Haidvogel (2004), Vertical mixing schemes in the coastal ocean: Comparison of the level 2.5 Mellor–Yamada scheme with an enhanced version of the K profile parameterization, *J. Geophys. Res. 109*, C01015, doi:10.1029/2002JC001702.
Feddersen, F. (2014), The generation of surfzone eddies in a strong alongshore current, *J. Phys. Oceanogr.*, *44*, 600–617, doi:10.1175/JPO-D-13-051.1.
Feddersen, F., and R. T. Guza (2003), Observation of nearshore circulation: Alongshore uniformity, *J. Geophys. Res.*, *108*(C1), 3006, doi:10.1029/2001JC001293.
Feddersen, F., R. T. Guza, S. Elgar, and T. H. C. Herbers (2000), Velocity moments in alongshore bottom stress parameterizations, *J. Geophys. Res.*, *105*, 8673 – 8686.
Feddersen, F., D. B. Clark, and R. T. Guza (2011), Modeling surf zone tracer plumes: 1. Waves, mean currents, and low-frequency eddies, *J. Geophys. Res.*, *116*, C11027, doi:10.1029/2011JC007210.
Fujimura, A. G., A. J. H. M. Reniers, C. B. Paris, A. L. Shanks, J. H. MacMahan, and S. G. Morgan (2014), Numerical simulations of larval transport into a rip-channeled surf zone, *Limnol. Oceanogr. Methods*, *59*, 1434–1447, doi:10.4319/lo.2014.59.4.1434.
Geiman, J. D., and J. T. Kirby (2013), Unforced oscillation of rip-current vortex cells, *J. Phys. Oceanogr.*, *43*, 477–497, doi:10.1175/JPO-D-11-0164.1.
Geiman, J. D., J. T. Kirby, A. J. H. M. Reniers, and J. H. MacMahan (2011), Effects of wave averaging on estimates of fluid mixing in the surf zone, *J. Geophys. Res.*, *116*, C04006, doi:10.1029/2010JC006678.
Haas, K. A., and I. A. Svendsen (2002), Laboratory measurements of the vertical structure of rip currents. *J. Geophys. Res.*, *107*(C5), 3047, doi:10.1029/2001JC000911.
Haas, K. A., I. A. Svendsen, M. C. Haller, and G. Zhao (2003), Quasi-three dimensional modeling of rip current system, *J. Geophys. Res.*, *108*(C7), 3217, doi:10.1029/2002JC001355.
Haller, M. C., and D. A. Dalrymple (2001), Rip current instabilities, *J. Fluid Mech.*, *433*, 161–192.
Hasselmann, K. (1971), On the mass and momentum transfer between short gravity waves and larger-scale motions, *J. Fluid Mech.*, *50*, 189–201.
Holman, R., and M. C. Haller (2013), Remote sensing of the nearshore, *Annu. Rev. Mar. Sci.*, *5*(1), 95–113.
Kennedy, A. B. (2003), A circulation description of a rip current neck, *J. Fluid Mech.*, *497*, 225–234.
Kumar, N., and F. Feddersen (2017a), The effect of Stokes drift and transient rip currents on the inner shelf. Part 1: No stratification, *J. Phys. Oceanogr.*, *47*, 227–241, doi:10.1175/JPO-D-16-0076.1.
Kumar, N., and F. Feddersen (2017b), The effect of Stokes drift and transient rip currents on the inner shelf. Part II: With Stratification, *J. Phys. Oceanogr.*, *47*, 243–260, doi:10.1175/JPO-D-16-0077.1.
Kumar, N., G. Voulgaris, J. C. Warner, and M. Olabarrieta (2012), Implementation of the vortex force formalism in the coupled ocean-atmosphere-wave-sediment transport (COAWST) modeling system for inner shelf and surf zone applications, *Ocean Modell.*, *47*, 65–95.
Kumar, N., F. Feddersen, Y. Uchiyama, J. McWilliams, and W. O'Reilly (2015), Midshelf to surfzone coupled ROMS–SWAN model–data comparison of waves, currents, and temperature: Diagnosis of subtidal forcings and response, *J. Phys. Oceanogr.*, *45*, 1464–1490, doi:10.1175/JPO-D-14-0151.1.
Large, W. G., J. C. McWilliams, and S. C. Doney (1994), Oceanic vertical mixing: A review and a model with nonlocal boundary layer parameterisation, *Rev. Geophys.*, *32*, 363–403.
Lesser, G. R., J. A. Roelvink, J. A. T. M. van Kester, and G. S. Stelling (2004), Validation and development of a three-dimensional morphological model, *Coastal Eng.*, *51*, 883–915.
Lippmann, T. C., and R. A. Holman (1990), The spatial and temporal variability of sand bar morphology, *J. Geophys. Res.*, *95*, 11,575–11,590.
Long, J. W., and H. T. Özkan-Haller (2009), Low-frequency characteristics of wave group-forced vortices, *J. Geophys. Res.*, *114*, C08004, doi:10.1029/2008JC004894.
Longuet-Higgins, M. S., and R. W. Stewart (1962), Radiation stress and mass transport in gravity waves, with application to 'surf beats,' *J. Fluid Mech.*, *13*, 481–504.
MacMahan, J., A. J. H. M. Reniers, E. B. Thornton, and T. Stanton (2004a), Infragravity rip current pulsations, *J. Geophys. Res.*, *109*, C01033, doi:10.1029/2003JC002068.

MacMahan, J., et al. (2010a), Mean Lagrangian flow behavior on an open coast rip-channeled beach: A new perspective, *Mar. Geol.*, *268*, 1–15.
MacMahan, J. H., A. J. H. M. Reniers, E. B. Thornton, and T. P. Stanton (2004b), Surf zone eddies coupled with rip current morphology, *J. Geophys. Res.*, *109*, C07004, doi:10.1029/2003JC002083.
MacMahan, J. H., E. B. Thornton, T. P. Stanton, and A. J. H. M. Reniers (2005), RIPEX: Observations of a rip current system, *Mar. Geol.*, *218*, 113–134.
MacMahan, J. H., A. J. H. M. Reniers, and E. B. Thornton (2010b), Vortical surf zone velocity fluctuations with *0*(10) min period, *J. Geophys. Res.*, *115*, C06007, doi:10.1029/2009JC005383.
Marchesiello, P., R. Benshila, R. Almar, Y. Uchiyama, J. McWilliams, and A. Shchepetkin (2015), On tridimensional rip current modeling, *Ocean Modell.*, *96*(1), 36–48, doi:10.1016/j.ocemod.2015.07.003.
McWilliams, J. C., J. M. Restrepo, and E. M. Lane (2004), An asymptotic theory for the interaction of waves and currents in coastal waters, *J. Fluid Mech.*, *511*, 135–178.
Mei, C. C. (1992), *The Applied Dynamics of Ocean Surface Waves*, 768 pp., World Sci., Singapore.
Munk, W. H. (1949), Surf beats, *Eos Trans. AGU*, *30*, 849–854.
Nairn, R. B., J. A. Roelvink, and H. N. Southgate (1991), Transition zone width and implications for modelling surfzone hydrodynamics, in *Proceedings of 22nd Int. Conf. Coastal Eng. 1990*, edited by B. L. Edge, pp. 68–82, Delft, Netherlands, Am. Soc. Civ. Eng., New York.
Newberger, P. A., and J. S. Allen (2007), Forcing a three-dimensional, hydrostatic, primitive-equation model for application in the surf zone: 2. Application to Duck94, *J. Geophys. Res.*, *112*, C08019, doi:10.1029/2006JC003474.
Noyes, T. J., R. T. Guza, S. Elgar, and T. H. C. Herbers (2004), Field observations of shear waves in the surf zone, *J. Geophys. Res.*, *109*, C01031, doi:10.1029/2002JC001761.
Oltman-Shay, J., P. A. Howd, and W. A. Birkemeier (1989), Shear instabilities of the mean longshore current: 2. Field observations, *J. Geophys. Res.*, *94*, 18,031–18,042.
Özkan-Haller H. T., and J. T. Kirby (1999), Nonlinear evolution of shear instabilities of the longshore current: A comparison of observations and computations, *J. Geophys. Res.*, *104*, 25,953–25,984.
Özkan-Haller, H. T., and Y. Li (2003), Effects of wave-current interaction on shear instabilities of longshore currents, *J. Geophys. Res.*, *108*(C5), 3139, doi:10.1029/2001JC001287.
Phillips, O. M. (1977), *The Dynamics of the Upper Ocean*. Cambridge Univ. Press, Cambridge, U. K.
Reniers, A. J. H. M., J. A. Battjes, A. Falqués, and D. A. Huntley (1997), A laboratory study on the shear instability of logngshore currents, *J. Geophys. Res.*, *102*, 8597–8609.
Reniers, A. J. H. M., J. H. MacMahan, E. B. Thornton, and T. P. Stanton (2007), Modeling of very low frequency motions during RIPEX, *J. Geophys. Res.*, *112*, C07013, doi:10.1029/2005JC003122.
Reniers, A. J. H. M., J. H. MacMahan, E. B. Thornton, T. P. Stanton, M. Henriquez, J. W. Brown, J. A. Brown, and E. Gallagher (2009), Surfzone surface retention on a rip channeled beach, *J. Geophys. Res. 114*, C10010, doi:10.1029/2008JC005153.
Reniers, A. J. H. M., J. H. MacMahan, F. J. Beron-Vera, and M. J. Olascoaga (2010), Rip-current pulses tied to Lagrangian coherent structures, *Geophys. Res. Lett.*, *37*, L05605, doi:10.1029/2009GL041443.
Ruessink, B., J. Miles, F. Feddersen, R. T. Guza, and S. Elgar (2001), Modeling the alongshore current on barred beach, *J. Geophys. Res.*, *106*, 22,451 – 22,463.
Shchepetkin, A. F., and J. C. McWilliams (2005), The Regional Oceanic Modeling System: A split-explicit, free-surface, topography-following-coordinate oceanic model. *Ocean Modell.*, *9*, 347–404.
Shchepetkin, A. F., and J. C. McWilliams (2008), Computational kernel algorithms for fine-scale, multiprocess, longtime oceanic simulations, in *Handbook of Numerical Analysis: Computational Methods for the Ocean and the Atmosphere*, edited by R. Temam and J. Tribbia, pp. 119–181, Elsevier, Amsterdam.
Smith, J. A. (2006), Wave–current interactions in finite-depth, *J. Phys. Oceanogr.*, *36*, 1403–1419.
Sonu, C. J. (1972), Field observations of nearshore circulation and meandering currents, *J. Geophys. Res.*, *77*, 3232–3247.
Spydell, M., and F. Feddersen (2009), Lagrangian drifter dispersion in the surf zone: Directionally spread, normally incident waves, *J. Phys. Oceanogr.*, *39*, 809–830.
Svendsen, I. A. (1984), Mass flux and undertow in a surf zone, *Coastal Eng.*, *8*, 347– 365.
Thornton, E. B., and R. T. Guza (1983), Transformation of wave height distribution, *J. Geophys. Res.*, *88*, 5925–5938.
Uchiyama, Y., and J. C. McWilliams (2008), Infragravity waves in the deep ocean: Generation, propagation, and seismic hum excitation, *J. Geophys. Res.*, *113*, C07029, doi:10.1029/2007JC004562.
Uchiyama, Y., J. C. McWilliams, and J. M. Restrepo (2009), Wave-current interaction in nearshore shear instability analyzed with a vortex-force formalism, *J. Geophys. Res.*, *114*, C06021, doi:10.1029/2008JC005135.
Uchiyama, Y., J. C. McWilliams, and A. F. Shchepetkin (2010), Wave-current interaction in an oceanic circulation model with a vortex force formalism: Application to the surf zone, *Ocean Modell.*, *34*, 16–35.
Walstra, D. J. R., J. A. Roelvink, and J. Groeneweg (2000), Calculation of wave-driven currents in a mean flow model, in *Coastal Engineering*, edited by B. L. Edge, pp. 1050–1063, Am. Soc. of Civ. Eng., Reston, Va.
Weir, B., Y. Uchiyama, E. M. Lane, J. M. Restrepo, and J. C. McWilliams (2011), A vortex-force analysis of the interaction of rip currents and gravity waves, *J. Geophys. Res.*, *116*, C05001, doi:10.1029/2010JC006232.
Yu, J. (2006), On the instability leading to rip currents due to wave-current interaction, *J. Fluid Mech.*, *549*, 403–428.
Yu, J., and D. N. Slinn (2003), Effects of wave-current interaction on rip currents, *J. Geopys. Res.*, *108*(C3), 3088, doi:10.1029/2001JC001105.
Zhao, Q., I. A. Svendsen, and K. Haas (2003), Three-dimensional effects in shear waves, *J. Geophys. Res.*, *108*(C8), 3270, doi:10.1029/2002JC001306.